

Dynamical dark energy: Current constraints and forecasts

Amol Upadhye¹, Moustapha Ishak², and Paul J. Steinhardt¹

¹ Department of Physics, Princeton University, Princeton, NJ 08544, USA

² Department of Astrophysical Sciences, Princeton University, Princeton, NJ 08544, USA

(Dated: May 23, 2019)

We consider how well the dark energy equation of state w as a function of red shift z will be measured using current and anticipated experiments. We use a procedure which takes fair account of the uncertainties in the functional dependence of w on z , as well as the parameter degeneracies, and avoids the use of strong prior constraints. We apply the procedure to current data from WMAP, SDSS, and the supernova searches, and obtain results that are consistent with other analyses using different combinations of data sets. The effects of systematic experimental errors and variations in the analysis technique are discussed. Next, we use the same procedure to forecast the dark energy constraints achievable by the end of the decade, assuming 8 years of WMAP data and realistic projections for ground-based measurements of supernovae and weak lensing. We find the 2 constraints on the current value of w to be $w_0(2) = 0.12$, and on dw/dz (between $z = 0$ and $z = 1$) to be $w_1(2) = 0.29$. Finally, we compare these limits to other projections in the literature. Most show only a modest improvement; others show a more substantial improvement, but there are serious concerns about systematics. The remaining uncertainty still allows a significant span of competing dark energy models. Most likely, new kinds of measurements, or experiments more sophisticated than those currently planned, are needed to reveal the true nature of dark energy.

PACS numbers: 98.80.Es, 98.65.Dx, 98.62.Sb

I. INTRODUCTION

Several years ago, observations of supernovae of type Ia (SN Ia) demonstrated that the expansion of the universe is accelerating [1, 2, 3, 4, 5]. Associated with this acceleration is dark energy, a component of the universe with negative pressure, that makes up a significant fraction of the total energy density. Recent years have seen the supernova evidence for dark energy continue to mount [6, 7, 8, 9, 10, 11]. Meanwhile, cosmological background (CMB) data from the WMAP project [12, 13], in combination with information about either the Hubble constant [14] or the galaxy power spectrum [15, 16], also requires the existence of dark energy. Cross-correlations between CMB anisotropies and matter power spectrum inhomogeneities provide evidence for a late-time integrated Sachs-Wolfe (ISW) effect [17, 18, 19, 20, 21, 22]. This ISW effect indicates a recent change in the inhomogeneous gravitational potential, providing further evidence for dark energy.

One way to characterize the dark energy is to measure its equation of state, the ratio $w = P/\rho$ of its pressure P and energy density ρ . The simplest model of the dark energy is a cosmological constant, which has a constant $w = -1$. Quintessence models describe the dark energy as a dynamical scalar field with an equation of state w

1, and in general, w will not be constant in time [23, 24, 25, 26]. Furthermore, models of extended quintessence or "phantom energy" even allow $w < -1$ [27]. Models of the universe incorporating a cosmological constant or quintessence, in addition to cold dark matter, are known as CDM or QCDEM models, respectively.

Discovering whether or not the dark energy is a cosmological constant is the primary goal of the study of dark

energy. If dark energy is shown not to be a cosmological constant, then the next important issues are whether or not $w < -1$, which can be theoretically problematic [28], and whether or not w is changing with time. While a quintessence with constant $w = -1$ is very difficult to distinguish quantitatively from a cosmological constant, the qualitative difference for fundamental physics is enormous, so it is critical that the maximum effort be made to reduce the uncertainty in w and its time derivative. Ultimately, the precise quantitative values of w and its time derivative are important for model building, but this is less crucial, at present, than the qualitative issue of whether the dark energy is dynamical or not. In order to address such questions about the nature of the dark energy, it is crucial that the equation of state and its time variation be determined observationally.

It has been known for some time that the cosmological probes used for studying the dark energy are plagued by numerous parameter degeneracies [29, 30, 31, 32, 33, 34, 35]. Because of these degeneracies, a large uncertainty in a cosmological parameter not directly related to the dark energy sector (e.g., the matter density) can lead to a large uncertainty in the dark energy equation of state. This sensitivity to other parameters means that one must incorporate the uncertainties in all parameters to obtain a realistic estimate of the uncertainties in the dark energy equation of state. In particular, one should avoid the use of strong priors on the form of $w(z)$, the values of other parameters, and independent information coming from other experiments. These can lead to underestimates of the uncertainty in w by a very large factor. We will also discuss how standard likelihood marginalization can give a misleading impression of the uncertainty in w .

The analysis presented here employs a χ^2 minimization procedure in order to avoid possible problems

with marginalization, and assumes only weak prior constraints. We compare our $^2\text{minimization}$ with the standard approach, the marginalization of a probability function computed using Monte Carlo Markov Chains. It is argued that our procedure gives a more conservative assessment of constraints in certain degenerate parameter spaces. In this sense, our procedure and the Markov Chain are complementary, as we will discuss.

We apply this $^2\text{minimization}$ analysis to the currently available data. The simultaneous determination of the dark energy equation of state and its red shift derivative is difficult without the combination of data from several cosmological probes. Thus we analyze the latest data from WMAP, SN Ia searches, and the Sloan Digital Sky Survey. Strong priors are avoided to prevent the underestimation of dark energy constraints. Although the data favor $w(0) < -1$ and $w'(0) > 0$, we are unable to rule out the cosmological constant conclusively. Furthermore, we find the constraints on $w(z)$ to depend strongly on the parametrization chosen for $w(z)$, as well as on the location of the best-fit model in parameter space, despite the fact that we have restricted our study to two-parameter equations of state. We also list possible biases in the cosmological probes, and discuss their effects on our results. Our conclusion that the cosmological constant is consistent with current data agrees with previous analyses, as we discuss in Sec. IV. This establishes the validity of our analytic methods, which we can then apply with confidence to projections of future measurements.

Since the cosmological constant is consistent with current data, it is useful to ask precisely how well dark energy may be constrained in the future using known cosmological probes. We address this question by applying our $^2\text{minimization}$ procedure to simulations of the data from these probes. Besides the CMB and SNe Ia, we simulate data from a probe of weak gravitational lensing (WL). In the future, WL is expected to be useful for constraining dark energy [36, 37, 38, 39, 40, 41, 42, 43, 44, 45, 46, 47, 48, 49]. Most of these studies have demonstrated that WL breaks parameter degeneracies in the CMB analysis, and have shown the effectiveness of the combination of CMB and WL data in constraining dark energy.

Our study is the first to use a joint analysis of simulated CMB, SNe Ia, and WL data, rather than imposing prior constraints as a "replacement" for one of these data sets. This is especially important for parameters such as $w(0)$ and $w'(0)$, which have strong degeneracies with other parameters. Since our goal is the study of $w(z)$ constraints, rather than general parameter constraints, we assume the cosmological model outside of the dark energy sector to be as simple as possible. Within this model, we are careful to avoid strong priors on the cosmological parameters. It is well understood that each of these cosmological probes has systematic uncertainties associated with it, and that significant progress needs to be made in order for each one to reach the level of precision necessary for constraining dark energy. Therefore,

we attempt at every opportunity to strike a reasonable balance between optimism and realism.

The paper is organized as follows. Sec. II A discusses several parametrizations of the dark energy equation of state. Our choice of cosmological parameters, and the prior constraints imposed on them, are listed in Sec. II B.

$^2\text{minimization}$ is compared with marginalization in Sec. II C. Sec. III A summarizes our analysis of current data, and Secs. III B - III D describe the simulation and analysis of future data. Finally, Sec. IV lists and interprets our findings, for our analysis of current data as well as our forecasts of future constraints, and Sec. V discusses our conclusions.

II. ANALYSIS METHODS

A. Dark energy parametrization

In the spirit of reasonable optimism, we have assumed that the dark energy may be parametrized using an equation of state $w(z) = P =$, where P and w are the pressure and dark energy density, respectively, and $w(z)$ is an unknown function of red shift. We have also assumed that the dark energy sound speed is $c_s^2 = 1$. Without any theoretical guidance about the form of $w(z)$, the space of all possibilities is equivalent to an uncountably infinite set of cosmological parameters. The data depend on $w(z)$ only through a multiple integral relation [35], so we lack the large number of measurements of $w(z)$ that would be necessary for non-parametric inference [50]. Thus we must describe $w(z)$ using a small number of parameters in order to keep the analysis tractable. The danger is that there is no "natural" way to parametrize $w(z)$, so the choice of parametrizations is essentially arbitrary. Ideally, one would like to verify that any constraints obtained on $w(z)$ are parametrization-independent. However, the space of all possible parametrizations is infinite-dimensional, so we're back to square one. The only feasible option is to test for parametrization-independence by comparing constraints on a small number of "reasonable-looking" parametrizations.

To begin with, we assume that $w(z)$ is an analytic function, and that it can be approximated at $z = 1$ by the first few terms in its Taylor series about $z = 0$. All known probes are sensitive to an integral of some function of $w(z)$, rather than to $w(z)$ itself, so any "bumps" and "wiggles" in $w(z)$ are effectively smoothed out. It is reasonable to assume that this smoothed $w(z)$ can be approximated by a low-degree polynomial in z out to $z < 1$. From now on we proceed based on this assumption, with the caveat that the "true" equation of state can have added "bumps and wiggles" that disappear when smoothed.

The simplest parametrizations useful for describing dynamical dark energy have at least two parameters, one describing the equation of state $w(0)$ at $z = 0$ and

$w(z)$	$w^0(0)$	$w^0 =$ $w(1) - w(0)$	$w(z)$ at $z = 1$
$w_0 + w^0 z$	w^0	w^0	divergent
$w_0 + \frac{w_a z}{(1+z)}$	w_a	$\frac{1}{2}w_a$	$w_0 + w_a$
$w_0 + \frac{w_a z}{(1+z)} + \frac{w_b z^2}{(1+z)^2}$	w_a	$\frac{1}{2}w_a + \frac{1}{4}w_b$	$w_0 + w_a + w_b$
$w_0 + w_1 z$ if $z < 1$ $w_0 + w_1$ if $z = 1$	w_1	w_1	$w_0 + w_1$

TABLE I: Summary of the dark energy equation of state parametrizations used in the literature.

the other parametrizing its red shift derivative $w^0(0) \frac{dw}{dz} \Big|_{z=0}$. A few parametrizations in the literature are

$$w(z) = w_0 + w^0 z \quad (\text{Simple parametrization}) \quad (1)$$

$$\begin{aligned} w(z) &= w_0 + (1 - a(z)) w_a \\ &= w_0 + \frac{w_a z}{1+z} \quad (\text{Ref. [51]}) \end{aligned} \quad (2)$$

$$\begin{aligned} w(z) &= w_0 + (1 - a(z)) w_a + (1 - a(z))^2 w_b \\ &= w_0 + \frac{w_a z}{(1+z)} + \frac{w_b z^2}{(1+z)^2} \quad (\text{Ref. [52]}) \end{aligned} \quad (3)$$

Note that w_a in (3) differs by a factor of 1 from the definition introduced in [52]. We chose (3) in order to facilitate comparison with (2) and (4). We are interested in the simplest two-parameter equations of state, and as we will see, (1) is of limited utility for studying high red shift data. This leaves only Eq. (2) out of the three parametrizations above. Since we would like to compare two "reasonable" two-parameter equations of state, we introduce a fourth parametrization,

$$w(z) = \begin{cases} w_0 + w_1 z & \text{if } z < 1 \\ w_0 + w_1 & \text{if } z = 1 \end{cases} \quad (4)$$

Dark energy constraints based on (4) and (2) may be compared in order to estimate the parametrization-dependence of our results. Table I compares all four parametrizations using their present-day derivatives $w^0(0)$, their mean low red shift ($0 < z < 1$) derivatives $w^0 = w(1) - w(0)$, and their high red shift limits $\lim_{z \rightarrow 1} w(z)$.

The high red shift limit of each parametrization becomes important when considering data from the CMB. Rather than providing information about $w(z)$ directly, the CMB data require only that the dark energy density be less than 10% of the critical density at the red shift $z_{\text{dec}} = 1100$ of photon decoupling [3, 54]. If $w(z) > 0$, the dark energy density will increase faster with red shift than the matter density, making the CMB constraint extremely difficult to satisfy. For the four dark energy parametrizations discussed above, the CMB effectively requires that $w(z) \leq 0$ at red shifts $z \geq 1$, that is, that the quantities listed in the fourth column of Table I are no greater than zero.

In each of the two- and three-parameter equations of state (1, 2, 3, 4), this high red shift constraint prevents

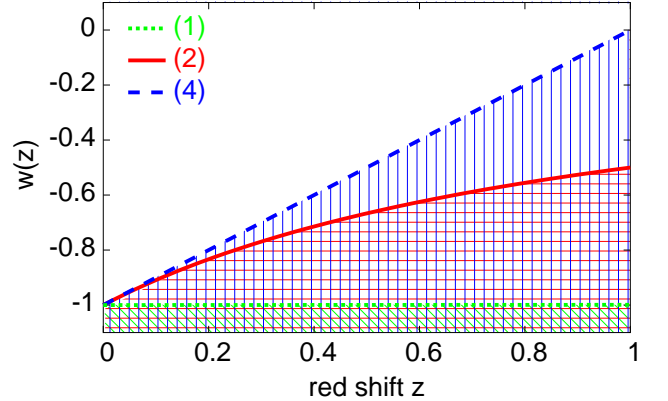


FIG. 1: Upper bounds on $w(z)$ for the three equations of state (4), (1), and (2). In all three cases, w_0 has been fixed at 1.

$w(z)$ from changing too rapidly at low red shifts. For fixed w_0 , we see that: $w^0 = 0$ in (1); $w_1 = w_0$ in (4); and $w_a = w_0$ in (2). In particular, w_1 and w_a have the same upper bound. Note that these bounds arise purely from the choice of parametrizations for $w(z)$. There is no fundamental physical reason for assuming that an equation of state which becomes positive at red shift $z = 1$ will stay that way long enough to interfere with the physics at decoupling.

Fig. 1 shows the upper bounds on the function $w(z)$ for each of the three parametrizations (1), (2), and (4), assuming $w_0 = 1$ in each case. Parametrization (1) disallows essentially all positive w^0 ; we will not study it further. Meanwhile, (2) allows $w(z)$ to increase by $w^0 = w(1) - w(0) = 0.5$, while (4) allows $w(z)$ to increase by $w^0 = 1$. Some parameter combinations such as $w_0 = 1, w^0 = 0.6$ are acceptable in (4), but are simply not allowed in (2). That is, the two parametrizations cover different regions in the (w, z) plane. Of course, these parametrization-dependent effects of the high red shift $w(z)$ constraint will be important only if the dark energy is found to have $w(z) > 0$ at $z = 1$.

We choose to use parametrization (4) for most of the subsequent work, since it allows the widest range of w^0 values. Equation (2) is also studied, and the results based on the two parametrizations are compared in order to estimate the parametrization dependence of our dark energy constraints. We describe the dynamics of the dark energy in terms of the ratio of the dark energy density to its value today,

$$Q(z) = \frac{w(z)}{w_0} = \frac{w(z) - w_0}{w_0} + 1 \quad (5)$$

For parametrization (4), the fluid continuity equation can be used to show that

$$Q(z) = \begin{cases} (1+z)^{3(1+w_0-w_1)} e^{3w_1 z} & \text{if } z < 1, \\ (1+z)^{3(1+w_0+w_1)} e^{3w_1(1-2\ln 2)} & \text{if } z = 1. \end{cases} \quad (6)$$

(A corresponding expression for equation of state (2) can be found in [51].) Given our assumption of a flat universe,

the Hubble parameter $H(z) = a$ evolves with red shift as follows.

$$H(z) = H_0 \frac{P}{m(1+z)^3 + (1-m)Q(z)} \quad (7)$$

These results will be used in our discussions of the cosmological probes.

B. Cosmological parameters, degeneracies, and priors

Cosmology may be described using a large number of parameters corresponding to a wide range of possible effects. The approach taken by, e.g., [16] is to test for as many of these effects as possible; they describe cosmology in terms of 13 parameters. On the other hand, our aim is more specific. We wish to determine whether dynamical dark energy will be distinguishable from a cosmological constant by the end of the decade. If we can answer this question in the negative after considering only a subset of these 13 parameters, then the addition of more parameters will not change our conclusions. We find that even with a relatively limited set of parameters we will not be able to rule out dynamical dark energy. Thus, in the interests of simplicity and computational efficiency, we restrict ourselves to nine parameters.

Outside of the dark energy sector, we choose the simplest possible description of the universe that is consistent with observations. The universe is assumed to be flat, and we do not include tensor modes, massive neutrinos, or primordial isocurvature perturbations. Besides the dark energy parameters w_0 and w_1 , our cosmological models are parameterized using: $h = H_0/(100 \text{ km sec}^{-1} \text{ Mpc}^{-1})$, where H_0 is the Hubble constant; $!_m = h^2 = \text{crit}$; $!_b = b h^2 = \text{crit}$; the optical depth to reionization; A , the normalization of the CMB power spectrum; n_s , the spectral index of the primordial power spectrum; z_s , the characteristic weak lensing source red shift. (The WL source red shift was shown to be important in, e.g., [55, 56, 57].) Actually, [16] shows that n_s is not absolutely necessary, since the simple Harrison-Peebles-Zeldovich spectrum ($n_s = 1$) fits the data well. However, n_s is a well-motivated parameter whose degeneracies with the dark energy parameters could be important. Borrowing the terminology of [16], we call $(h, !_m, !_b, A, n_s, z_s)$ the "vanilla" parameters. Thus, our analysis adds to the simple "vanilla" model one parameter describing weak lensing sources, and two parameters describing the dark energy.

Our constraints based on this limited set of parameters will be optimistic, since including more parameters will tend to increase the uncertainties in w_0 and w_1 . This is especially true when the parameters that we neglect are highly correlated with some of the parameters that we do consider. Ref. [16] shows a strong degeneracy between the Hubble parameter h and the curvature κ that could potentially affect our dark energy constraints. Also, [37] points out that neutrinos become important

when using weak lensing in the nonlinear regime to study dark energy.

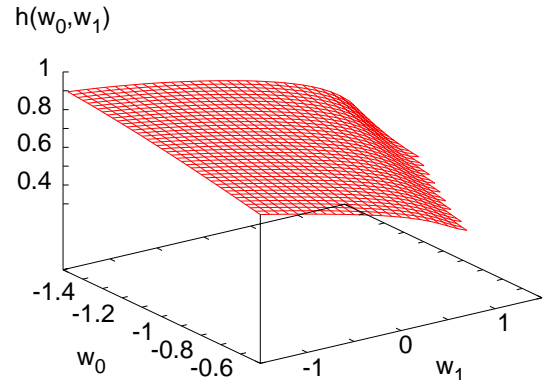


FIG. 2: $h(w_0, w_1)$ satisfying the CMB angular diameter distance degeneracy, with parameters $!_m = 0.14$, $z_{\text{dec}} = 1089$, and $d_{\text{AC}}^{(\text{dec})} = 14.0 \text{ Gpc}$ fixed to their WMAP [12] values.

Even in our relatively simple parameter space, there exist several parameter degeneracies. That is, to each point in parameter space there corresponds a degenerate region of observationally indistinguishable points. A degeneracy that is particularly important to the study of dark energy is the angular diameter distance degeneracy [30, 32, 33, 34]. For universes containing matter and a dark energy of the form (4), this implies that models with the same values of $!_m$, $!_b$, and the comoving angular diameter distance $d_{\text{AC}}^{(\text{dec})}$ to the decoupling surface, will produce indistinguishable CMB power spectra. $d_{\text{AC}}^{(\text{dec})}$ as a function of h , w_0 , and w_1 is given by

$$d_{\text{AC}}^{(\text{dec})}(h; w_0, w_1) = c \int_0^{z_{\text{dec}}} \frac{dz^0}{H(z^0)} \quad (8)$$

where $H(z^0)$ is given by (7). Even when $!_m$ is fixed, each choice of w_0 and w_1 has a corresponding h for which this degeneracy is satisfied, as shown in Fig. 2. Other important degeneracies include the large-scale CMB degeneracy [29] among $!_m$, $!_b$, n_s , and $w(z)$; the small-scale CMB degeneracy [31] among A , and n_s ; and the supernova luminosity distance degeneracy [35] between $!_m$ and $w(z)$. The presence of these parameter degeneracies means that we must combine several cosmological probes in order to obtain reliable constraints. Furthermore, combinations of known probes contain residual degeneracies, which we must deal with carefully in order to determine constraints on the dark energy.

In order to make a fair assessment of parameter degeneracies, it is necessary to avoid strong prior constraints on the cosmological parameters. We have been careful to use very weak priors. The dark energy equation of state is required to be negative or zero at all red shifts, $w(z) \leq 0$. For the model (4), this implies the two prior constraints $w_0 \leq 0$ and $w_0 + w_1 \leq 0$. For physical reasons, we must assume $0 < !_m < 1$, $!_b < !_m$, $A > 0$, and $z_s > 0$. Besides these, the constraints $0.4 < h < 1.1$, $0.003 < !_b$,

Parameter	Lower Bound	Upper Bound
h	0.4	1.1
$!_b$	0.003	$!_m$
$!_m$	$!_b$	1
m	0	1
K	0	0
	0	1
A	0.5	1.5
n_s	0.5	1.5
z_s	0	1.5
w_0	N/A	0
$w_0 + w_1$	N/A	0

TABLE II: Summary of the prior constraints assumed for the grid minimization analysis.

$!_m < 1$, $m < 1$, $0.5 < A < 1.5$, $0.5 < n_s < 1.5$, and $z_s < 1.5$ are imposed for computational convenience. The above priors are summarized in Table II.

The simulated data sets used here for constraint forecasts assumed a fiducial model $w_0 = -1$, $w_1 = 0$, $h = 0.7$, $!_m = 0.15$, $!_b = 0.023$, $m = 0.1$, $A = 0.8$, $n_s = 1$, $z_s = 1$. This roughly corresponds to the "vanilla lite" CDM model of [16], with lensing sources assumed to be at characteristic red shift 1. Our chosen fiducial model implies $m = 0.31$, $!_b = 0.047$, and $z_s = 0.92$.

C. χ^2 minimization

In order to provide an accurate picture of the dark energy constraints in a degenerate parameter space, a χ^2 minimization procedure was used. Constraints on the dark energy parameters were determined using the 1 and 2 contours of the χ^2 function in the (w_0, w_1) plane. At any given point (w_0, w_1) , $\chi^2(w_0, w_1)$ was computed by minimizing over all other cosmological parameters.

χ^2 minimization handles certain types of degeneracies more carefully than marginalization, the procedure most commonly used to obtain cosmological constraints, meaning that the two methods are complementary. Marginalization favors models that fit well over "large" regions of parameter space. Given two cosmological models with the same low χ^2 , marginalization will give extra weight to the model that sits in a large region of low- χ^2 models. Meanwhile, χ^2 minimization will pick the best model while completely ignoring its surroundings. These differences are illustrated in Fig. 3, based on a sample χ^2 function of two arbitrary parameters x and y . The 1σ contour of $\chi^2(x; y)$ is shown in Fig. 3 (top). Note that the contour has a small slope at low x , but is nearly parallel to the y axis at high x .

If we are interested only in constraints on x , then we can either minimize or marginalize over y . Fig. 3 (mid) sketches the probability functions obtained using the two different methods. Consider the two models A and B, at x_A and x_B respectively, whose y values are chosen to

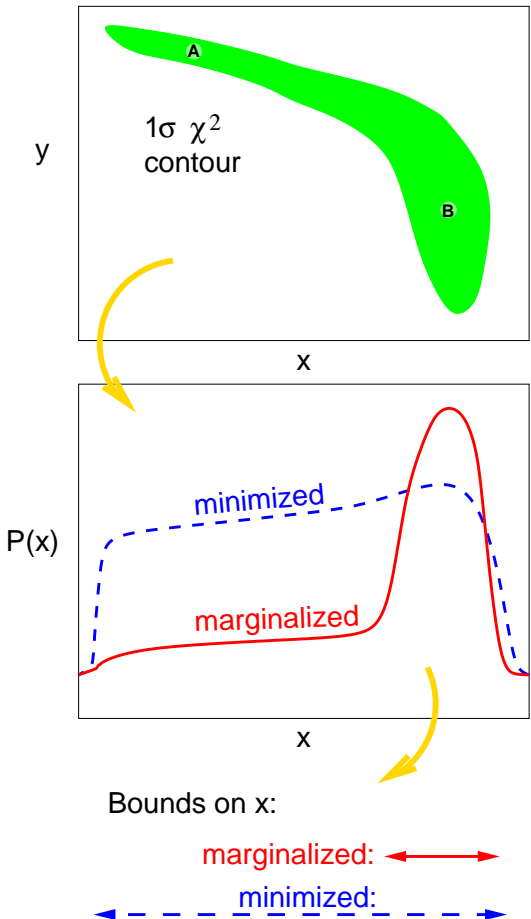


FIG. 3: Comparison of minimization and marginalization in a (hypothetical) degenerate parameter space. Two models, A and B, are labelled. (top): Sample 1σ contour of $\chi^2(x; y)$ in a degenerate parameter space. (mid): Probability functions based on minimization and marginalization. The probability based on minimization (dashed line) is $P_{\text{min}}(x) / \exp \chi^2(x; y)$. The marginalized probability (solid line) is $P_{\text{marg}}(x) / \int \exp \chi^2(x; y) P_{\text{prior}}(x; y) dy$. (bot): Constraints on x based on minimized and marginalized probability functions.

minimize $\chi^2(x; y)$ at the corresponding x values. Minimization takes the viewpoint that, since $\chi^2_A = \chi^2_B$, the x values x_A and x_B are approximately equally probable. On the other hand, marginalization assigns a much greater probability to x_B , since there are many more low- χ^2 models at x_B than at x_A . Thus the χ^2 -minimized probability distribution looks like a broad plateau, while the marginalized probability looks like a sharp peak with a "shoulder." The bounds on x obtained from these two methods, as shown in Fig. 3 (bot), are quite different. Note that this discussion is not just academic. The CMB 95% probability contour in the (h, Ω_{tot}) plane, shown in Fig. 7 of [16], is qualitatively very similar to the contour shown here in Fig. 3 (top).

The parameter bounds derived from marginalization

contour	n^2	n^2_{in}	probability
n	n^2		
1	1	39.3%	
1.52	2.3	68.3%	
2	4	86.5%	
2.49	6.2	95.5%	

TABLE III: Comparison between n^{-2} contours and probability contours for a Gaussian likelihood function of two variables.

have excluded models such as A, which are within the n^{-2} contour, simply because the low- n^{-2} regions at their x values are "thin" in the y direction. A procedure that excludes such "thin-contour" models, in favor of "thick-contour" models such as B, can be problematic for two reasons. First of all, it is not clear that low- n^{-2} models such as A really should be ignored; it is prudent, at least, to know of the existence of such a model. Points at the ends of long, narrow regions of degeneracy are "thin-contour" points, so marginalization can underestimate the sizes of these degenerate regions. Such points should be considered in a proper treatment of parameter degeneracies.

Secondly, the notions of "thinness", "thickness", and "distance" in parameter space depend on the prior constraints chosen. For a parameter vector p of N parameters, the a posteriori probability marginalized over all but m of the parameters is given by

$$Z$$

$$P(p^0; \dots; p^{m-1}) = \int dp^m \dots dp^N L(p) P_{\text{prior}}(p) \quad (9)$$

It is customary to reduce this dependence on priors by choosing uniform priors, with $P_{\text{prior}}(p)$ constant on a subset of parameter space and zero elsewhere. However, the concept of uniform priors is itself parameterization-dependent. Choosing priors that are uniform in a different set of parameters q is equivalent to letting $P_{\text{prior}}(p)$ equal the Jacobian determinant of the transformation from p to q .

On the other hand, marginalization has several advantages of its own. First of all, one can always come up with a $\chi^2(x; y)$ function which is handled correctly by marginalization, but for which minimization implies artificially tight constraints. Also, marginalization naturally defines a probability in parameter space. An analysis based on marginalization is capable of providing probability contours, which may be more useful than n^{-2} contours. If the likelihood function is Gaussian, these two types of contours are related in a simple way, as shown in Table III. However, for a non-Gaussian likelihood function, there is no simple way to relate contours of $\chi^2(p)$ to a given probability contour without marginalization. Meanwhile, it may be the case that a "natural" set of parameters exists for describing a theory, such as h , m , and b , in general relativistic cosmology. The existence of "natural" parameters makes it easier to choose a "reasonable"

"prior probability distribution P_{prior} ", since one no longer needs to worry about reparameterization changing the form of P_{prior} . Constraints derived from a marginalization over such parameters, assuming weak and uniform priors, can be quite convincing.

We take the point of view that any natural constraints on w_0 and w_1 should be independent of the analysis method used. If a claim made using one of the two methods does not hold up to scrutiny by the other method, then the issue is too close to call. For example, we do not believe that model A in Fig. 3 is ruled out, even though it is excluded by marginalization over y . In this sense,

n^{-2} minimization and marginalization are complementary analysis techniques that are useful for handling different types of parameter degeneracies in a non-Gaussian likelihood function. We have chosen to use n^{-2} minimization, partly because we are concerned about degenerate regions such as in 3 (top), and partly because it is not clear which parameters should be used to describe dark energy, reionization (z_{reion}), and the power spectrum amplitude (A or s).

For completeness, we discuss a few computational issues here. Minimizations were performed using the Amoeba routine of [58], although the Powell routine from that reference was found to give very similar results. The computation was sped up by generating CMB power spectra for 100 different n_s values at once, and interpolating to find n^2 for intermediate n_s values. This gave us information about n^2 over our entire range of n_s values with just one call to CMBFAST. (Interpolation-related errors in n^2 were found to be negligible.) Also, we minimized separately over the three parameters A , n_s , and z_s , since a variation in one of these parameters did not require the recomputation of CMB power spectra. This minimization over A , n_s , and z_s was nested within the minimization over h_m , h_b , and b . Using this technique, n^2_{CMB} could be minimized at one point in the (w_0, w_1) plane in about 2–4 hours, on a single node of the Hydra computer cluster.

III. COSMOLOGICAL PROBES

A. Current data

Since our analyses of current data follow standard procedures, we will discuss them only briefly.

Supernovae of Type Ia: Supernovae of type Ia (SN Ia) are standardizable candles [59, 60, 61, 62], with magnitude $m(z)$ at redshift z given in, e.g., [63], by

$$m = 5 \log_{10}(D_L) + M \quad (10)$$

The dimensionless luminosity distance $D_L(z) = (1+z)H_0 \int_0^z dz^0 H(z^0)$ depends on m and the dark energy parameters through $H(z)$, given in (7). Our analysis minimizes n^2 with respect to the magnitude parameter M , which is dependent on H_0 and the SN Ia absolute magnitude.

Cosmic Microwave Background: For the dynamical models of dark energy considered here, power spectra were computed with a modified version of CMBFAST 4.1 [64], provided by R. Caldwell [65]. Our analysis of the data used our own implementation of the CMB Ω^2 function described in [66]. Noise parameters and constants describing the WMAP parameterization of the Fisher matrices were taken from the data tables created by [67] and [68], and provided with the WMAP likelihood code.

Galaxy Power Spectrum: Our analysis of Sloan Digital Sky Survey (SDSS) data used the galaxy power spectrum [15] and the likelihood code of [16], made publically available at [69]. Given a cosmological model, the corresponding matter power spectrum was computed using CMBFAST. The normalization of the power spectrum was treated as a nuisance parameter; Ω^2 was minimized with respect to it. An accurate formula for the matter power spectrum in the nonlinear regime, for dynamical dark energy cosmologies, is not currently available. Furthermore, galaxy biasing in the nonlinear regime is even less well understood. Therefore, the SDSS data analysis presented here only used measurements for $k = 0.15 \text{ h Mpc}^{-1}$, as recommended in [16].

B. SN Ia Simulation

1. Supernova simulation strategies

Monte Carlo techniques were used to simulate the magnitudes and red shifts of Type Ia Supernovae, from previous, current, and future supernova surveys, that would be available for analysis by the end of the decade. Rather than mixing real and simulated data, it was decided to simulate all of the surveys from scratch. In order to conduct a realistic simulation of future supernova surveys, we studied the available literature, including analyses of current data as well as plans for future surveys. For each SN Ia survey we estimated the expected number of supernovae to be observed and modeled a SN Ia red shift distribution. The simulated SN Ia data set included 2239 supernovae ranging in red shift from 0.01 to 1.6, as summarized in Table IV. Our simulation was based upon the following assumptions, which we justified by reference to data whenever possible.

25% of the SNe Ia found by each survey were assumed to be unusable for cosmological analysis. This is based on the fact that 23% of the SNe Ia in the Tonry/Barris data set [8, 10] did not survive their cuts on very low red shifts ($z < 0.01$) and galactic host extinctions.

Two-thirds of all low red shift SNe (of all types) were assumed to be of type Ia, based on the supernovae reported in [70].

Red shift distributions were assumed to be uniform for low red shifts. Since $m(z)$ at low red shifts

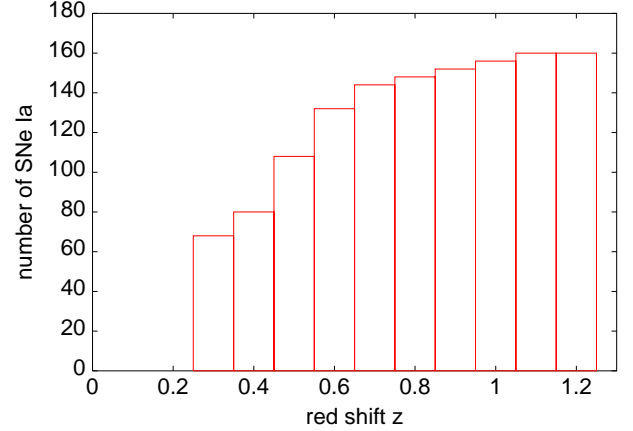


FIG. 4: Red shift distribution of the SNe Ia supernovae, shown in bins of width $z = 0.1$.

is independent of cosmological parameters other than M , the details of the red shift distribution for $z < 0.1$ should be unimportant for parameter constraints.

Red shift distributions were assumed to be Gaussian ($P(z) \propto \exp\left(-\frac{(z - z_{\text{mean}})^2}{2\sigma_z^2}\right)$) for higher red shift surveys, unless otherwise specified in the literature.

Current data reported in [8, 9, 10, 11] were simulated by dividing them into three surveys:

- low z , Tonry/Barris SNe Ia with $z < 0.1$;
- mid z , SNe Ia from [8, 9, 10] with $z > 0.1$;
- high z , HST GOODS SNe Ia [11].

This was done because the current data come from a collection of previous surveys over a wide range of red shifts, and are poorly approximated by uniform or Gaussian distributions.

40% of the expected Dark Energy Camera [71] data were assumed to be available, bringing the total number of supernovae to just over 2000. Even under optimistic assumptions about systematic uncertainties, we do not expect an increase in the number of SNe beyond this point to improve constraints on dark energy [72].

2. Magnitude uncertainties

A well-studied SN Ia sample, with accurate spectroscopic measurements of the supernova host galaxy red shifts, can have a magnitude uncertainty for each supernova as low as 0.15 [71, 73]. If less accurate host red shift information is available, the magnitude uncertainty

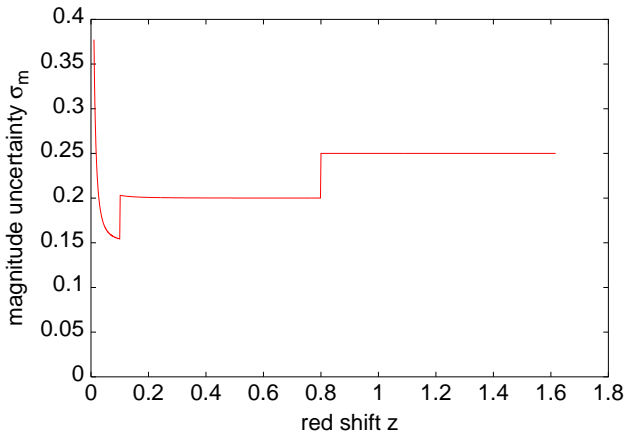


FIG. 5: Supernova apparent magnitude uncertainty used in the simulation

users; [71] estimates an uncertainty of 0.25 when only photometric red shift information is available for the host galaxies. Meanwhile, the average magnitude uncertainty in the Tonry/Barris sample, for SNe Ia in the red shift range $0.1 < z < 0.8$, is 0.3. Since the final dataset will be a combination of many supernovae with varying amounts of red shift information, the approach adopted here is to assume a magnitude uncertainty of 0.2 for supernovae in the intermediate red shift range $0.1 < z < 0.8$.

Judging from the supernovae tabulated in [8] and [10], the low red shift supernovae tend to have smaller magnitude uncertainties than average. The mean magnitude uncertainty is 0.18 for the $z < 0.1$ SNe Ia, compared to 0.25 for the full Tonry/Barris sample. Thus, for the purposes of this simulation, it is assumed that the magnitude uncertainty for each low red shift ($z < 0.1$) supernova is the minimum value, 0.15.

Meanwhile, supernovae at red shifts greater than about $0.8 - 1.0$ become increasingly difficult to observe from the ground, and the spectroscopic analyses of such SNe Ia become very time-consuming [73, 74]. In the Tonry/Barris sample, the magnitude uncertainty rises from a mean of 0.3 in the red shift range $0.1 < z < 0.8$ to 0.35 in the range $z > 0.8$. Based on this, it was decided to assume a magnitude uncertainty of 0.25 for supernovae with $z > 0.8$.

Finally, a peculiar velocity uncertainty was added to each of the errors assumed above. Following [8], it was assumed here that the peculiar velocity uncertainty of each supernova was $v = 500 \text{ km/sec}$. That is, the fractional uncertainty in the luminosity distance due to the peculiar velocity uncertainty was taken to equal the fractional uncertainty $\frac{v/c}{z}$ in red shift. Thus,

$$s_m = \sqrt{\frac{1}{5} s_m^{\text{uncorrected}} + \frac{v^2}{\ln(10) c^2 z^2}}; \quad (11)$$

where c is the speed of light. This is a form of the magnitude uncertainty, after correction for peculiar velocities,

SN Ia data set	number of SNe Ia	red shift distribution
Current (low z) [8, 10]	83	uniform, $0.01 < z < 0.1$
Current (mid z) [8, 9, 10]	117	Gaussian, $z_{\text{mean}} = 0.55, z = 0.25$
Current (high z) [11]	16	Gaussian, $z_{\text{mean}} = 1.0, z = 0.4$
SN factory [70]	225	uniform, $0.01 < z < 0.1$
SDSS [75]	100	uniform, $0.05 < z < 0.15$
SNLS [73, 76, 77]	978	see Fig. 4
ESSENCE [78, 79, 80]	150	uniform, $0.15 < z < 0.75$
DECam era [71]	570	Gaussian, $z_{\text{mean}} = 0.55, z = 0.25$
Total	2239	

TABLE IV : Numbers and red shift distributions of simulated type Ia supernovae.

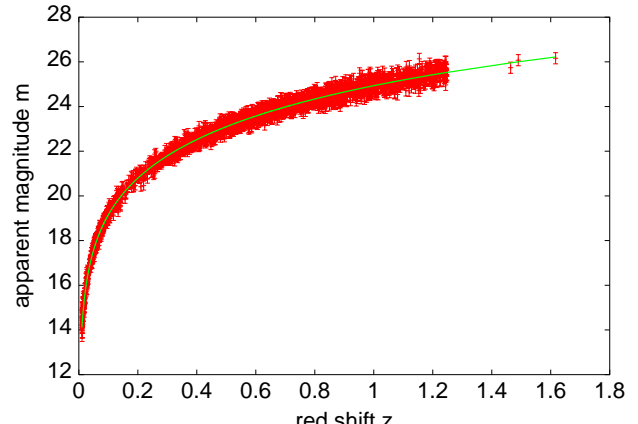


FIG. 6: The simulated SN Ia dataset. The points with error-bars are the simulated supernovae, while the solid line is the fiducial model.

is plotted in Fig. 5.

3. The complete SNe Monte Carlo dataset

Monte Carlo supernova "data" points were generated using the red shift distributions and magnitude uncertainties specified above. For each supernova from each simulated experiment, the appropriate red shift distribution was used for the random generation of a red shift z . To be specific, the red shift probability distribution $P_i(z)$ for each experiment i was first normalized so that its maximum value was 1. Then, two random numbers, r_1 and r_2 , were chosen from a uniform distribution between 0 and 1. If the probability $P_i(z_{\text{max}} r_1)$ at red shift $z_{\text{max}} r_1$

was greater than r_2 , then $z_{\text{max}} r_1$ was taken to be the red shift of the supernova. Otherwise, the two numbers were discarded and the process repeated. Here, z_{max} , the maximum allowed supernova red shift, was set to 2.0 for each experiment.) Next, the apparent magnitude $m^{(\text{fid})}(z)$ expected for a supernova at red shift z was computed for the fiducial model used here: $m = 0.31$, $w_0 = -1$, $w_1 = 0$. The magnitude uncertainty $\sigma_m(z)$ for that supernova was chosen as described in the previous subsection. Finally, the simulated apparent magnitude $m^{(\text{MC})}$ was computed by adding to $m^{(\text{fid})}(z)$ a random number chosen from a Gaussian distribution, with mean zero and standard deviation $\sigma_m(z)$. These Monte Carlo simulated magnitudes $m^{(\text{MC})}$, along with their corresponding red shifts and magnitude uncertainties, formed the simulated dataset used here.

Table IV lists the numbers and red shift distributions of the supernovae simulated, and Fig. 6 plots the magnitude-red shift relation of the simulated "data". Note that, since the major supernova surveys planned over the next several years are ground-based, the simulated dataset contains very few supernovae with red shift greater than about 1.2.

C. CMB Simulation

1. CMB covariance matrix

In the following discussion, we use the convention of [81] that $C_l = 1/(l+1)C_{l-1}$ for any power spectrum C_l . We computed variances in the C_l s using the expressions given in [66] and [68] for the diagonal components of the covariance matrices. The noise parameters N_1^{TT} and N_1^{EE} were defined to be 1/8 of those used by WMAP, in order to simulate the effects of using eight years of WMAP data. WMAP noise parameters were taken from their data tables, which were described in [67] and [68], and provided along with the WMAP likelihood code described in [66]. The effective noise parameter $N_1^{\text{TT};(\text{eff})}$ as a fraction of the original noise parameter N_1^{TT} , and the effective sky fraction $f_{\text{sky}}^{(\text{eff})}(l)$, were defined as in [66]. The final expression for the uncertainties in the C_l^{TT} s was therefore taken to be

$$p \frac{C_l^{\text{TT};(\text{theory})}}{\text{Var}(\text{TT})} = \frac{C_l^{\text{TT};(\text{theory})} + N_1^{\text{TT};(\text{eff})}}{(1 + \frac{1}{2})f_{\text{sky}}^{(\text{eff})}} : \quad (12)$$

Note that (12) is a more conservative expression for the variance than that given by [81], since there is an "extra" factor of f_{sky} in the denominator of $\text{Var}(\text{TT})$. The information "lost" by dividing $\text{Var}(\text{TT})$ by f_{sky} is actually stored in the off-diagonal components of the covariance matrix (which we ignored), because nearby C_l s are anti-correlated [66]. However, we found that this extra f_{sky} had only a negligible effect on our forecast constraints.

We used a similar form for the uncertainty in the E-mode polarization power spectrum C_l^{EE} . Since WMAP

did not include the C_l^{EE} s in the likelihood analysis of their first year data, effective corrections to the noise and sky fraction were not computed. We used $f_{\text{sky}} = 0.85$ and $N_1^{\text{EE};(\text{eff})} = N_1^{\text{EE}}$.

$$p \frac{C_l^{\text{EE};(\text{theory})}}{\text{Var}(\text{EE})} = \frac{C_l^{\text{EE};(\text{theory})} + N_1^{\text{EE}}}{(1 + \frac{1}{2})f_{\text{sky}}^2} \quad (13)$$

Finally, uncertainties for the cross-power spectrum C_l^{TE} were taken from Eq. (10) in [68], using $f_{\text{sky}} = 0.85$ and $f_{\text{sky}}^{\text{TE};(\text{eff})} = \frac{f_{\text{sky}}}{1.14}$ as described in that reference.

$$\text{Var}(\text{TE}) = \frac{(C_1^{\text{TT}} + N_1^{\text{TT}})(C_1^{\text{EE}} + N_1^{\text{EE}}) + (C_1^{\text{TE}})^2}{(2l+1)f_{\text{sky}}f_{\text{sky}}^{\text{TE};(\text{eff})}} \quad (14)$$

Even in the absence of a sky cut, correlations exist among the three power spectra C_l^{TT} , C_l^{TE} , and C_l^{EE} for each l [31]. As above, we include an "extra" factor of f_{sky} in the denominators of the expressions given in that reference. For a given multipole l , the covariance matrix C_{XX} , where $X;Y = \text{TT}; \text{TE}; \text{EE}$, is given by,

$$C_{XX}^{(1)} = \text{Var}(X) \quad (15)$$

$$C_{\text{TT};TT}^{(1)} = \frac{(C_1^{\text{TT}} + N_1^{\text{TT}})C_1^{\text{TE}}}{(1 + \frac{1}{2})f_{\text{sky}}^2} \quad (16)$$

$$C_{\text{TT};EE}^{(1)} = \frac{(C_1^{\text{TE}})^2}{(1 + \frac{1}{2})f_{\text{sky}}^2} \quad (17)$$

$$C_{\text{TE};EE}^{(1)} = \frac{(C_1^{\text{EE}} + N_1^{\text{EE}})C_1^{\text{TE}}}{(1 + \frac{1}{2})f_{\text{sky}}^2} \quad (18)$$

Large- l correlations are also expected to exist between the CMB power spectra and large scale structure, due to the Sunyaev-Zeldovich effect [82, 83] and the gravitational lensing of the CMB [84, 85]. However, these effects are too small to detect today [86, 87, 88]. The analysis presented here neglected such correlations. In particular, we assumed the CMB \mathcal{C}_l^2 function to be independent of the red shifts z_s of weak lensing sources.

2. Simulation

A set of simulated TT, TE, and EE CMB power spectra was generated by means of a Monte Carlo simulation. For the purposes of this simulation, it was assumed that the WMAP project [12] would be extended to eight years. Data from the Planck mission, as described in [89] and [90], were not simulated for this work; the analysis of Planck data will be complicated by nonlinear effects such as the gravitational lensing of the power spectra.

The WMAP-8 data set described here contained eight years of simulated WMAP data. We simulated TT data up to a maximum multipole of $l_{\text{max}}^{\text{TT}} = 900$, and TE and EE data up to $l_{\text{max}}^{\text{EE}} = 512$. As detailed above, we divided

by eight the tabulated WMAP noise parameters from one year of data. Given the CMBFAST-generated ducial power spectra $C_1^{TT;fid}$, $C_1^{TE;fid}$, and $C_1^{EE;fid}$, as well as our simulated noise parameters, the power spectrum covariance matrices (15-18) were computed. For each l , the inverse covariance matrix $C^{(1)}^{-1}$ was diagonalized,

$$D^{(1)} = U^{(1)} C^{(1)} U^{(1)} = \begin{pmatrix} 0 & \frac{1}{(u_1^1)^2} & 0 & 0 & 1 \\ 0 & 0 & \frac{1}{(u_1^2)^2} & 0 & C \\ 0 & 0 & 0 & \frac{1}{(u_1^3)^2} & \end{pmatrix}; \quad (19)$$

using the matrix $U^{(1)}$ of eigenvectors of $C^{(1)}^{-1}$. Next, $U^{(1)}$ was used to rotate the vector of ducial power spectra into the eigenbasis,

$$\begin{pmatrix} 0 & 1 & 0 & C_1^{TT;fid} & 1 \\ 0 & u_1^2 A & U^{(1)} B & C_1^{TE;fid} & C \\ u_1^2 A & 0 & 0 & C_1^{EE;fid} & A \\ u_1^3 & C_1^{EE;fid} & 0 & 0 & \end{pmatrix}; \quad (20)$$

The Monte Carlo simulated power spectra were generated in the eigenbasis, using random numbers r_1 , r_2 , and r_3 chosen from a Gaussian distribution with zero mean and unit variance:

$$u_1^{1;MC} = u_1^1 + r_1 u_1^1 \quad (21)$$

$$u_1^{2;MC} = u_1^2 + r_2 u_1^2 \quad (22)$$

$$u_1^{3;MC} = u_1^3 + r_3 u_1^3 \quad (23)$$

Finally, the Monte Carlo power spectra were rotated back into the standard basis,

$$\begin{pmatrix} 0 & C_1^{TT;MC} & 1 & 0 & u_1^{1;MC} & 1 \\ 0 & C_1^{TE;MC} & C & U^{(1)} B & u_1^{2;MC} & C \\ C_1^{TE;MC} & 0 & 0 & U^{(1)} C & u_1^{3;MC} & A \\ C_1^{EE;MC} & C & A & 0 & u_1^1 & \end{pmatrix}; \quad (24)$$

These final simulated power spectra, $C_1^{TT;MC}$, $C_1^{TE;MC}$, and $C_1^{EE;MC}$, were the ones used in our analysis. Note that this simulation method ignores non-Gaussianities in the distributions of observed C_1 values about the underlying model; see [81] for a discussion of such effects. The simulated TT, TE, and EE power spectra are shown in Figs. 7, 8, and 9, respectively.

D. Weak Lensing Simulation

1. Convergence power spectrum

In the Limber approximation, the convergence power spectrum is given by [91, 92, 93]:

$$P_1 = \frac{9}{4} H_0^4 \frac{a^2}{m} \frac{g^2(\ell)}{a^2(\ell)} P_{3D} \frac{1}{\sin_K(\ell)}; \quad d; \quad (25)$$

where P_{3D} is the 3D nonlinear power spectrum of the matter density fluctuation, d ; $a(\ell)$ is the scale factor;

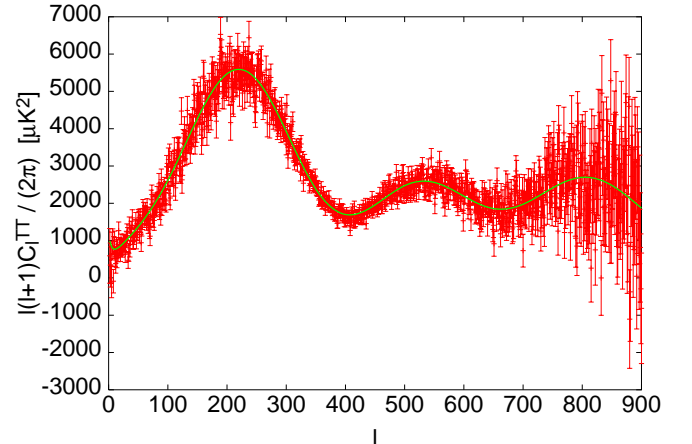


FIG. 7: WMAP-8 simulated TT power spectrum. The points with errorbars are the simulated 'data', while the solid line is the ducial model.

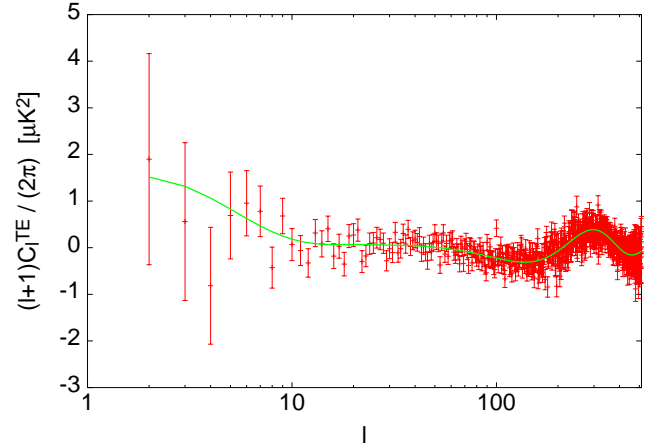


FIG. 8: WMAP-8 simulated TE power spectrum. The points with errorbars are the simulated 'data', while the solid line is the ducial model.

and $\sin_K = K^{1/2} \sin(K^{1/2})$ is the comoving angular diameter distance to (for the spatially flat universe used in this analysis, this reduces to d). The weighting function $g(\ell)$ is the source-averaged distance ratio given by

$$g(\ell) = \frac{Z}{n(z)} \frac{\sin_K(0)}{\sin_K(z)} d(0); \quad (26)$$

where $n_K(z)$ is the source red shift distribution normalized by $dz n(z) = 1$. We assume that all the sources are at a characteristic red shift z_s , so that (26) reduces to

$$g(\ell) = \frac{\sin_K(z_s)}{\sin_K(0)}; \quad (27)$$

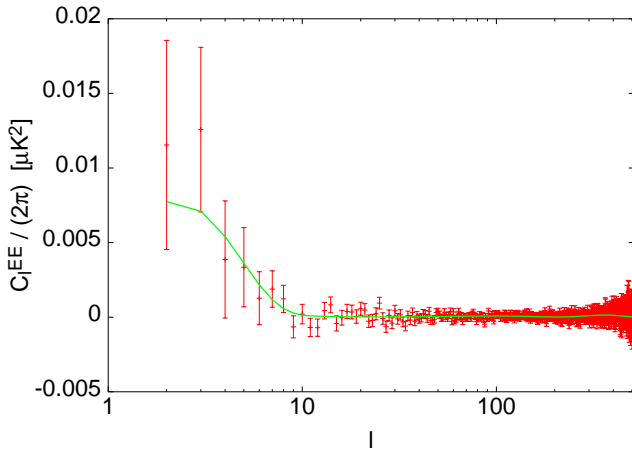


FIG. 9: WMAP-8 simulated EE power spectrum. The points with errorbars are the simulated "data", while the solid line is the fiducial model. Note that some of the errorbars at $l > 300$ extend beyond the bounds of the displayed plot.

For weak lensing calculations, we use the standard BBKS transfer function [94], and the analytic approximation of Ref. [95] for the growth factor. We use the mapping procedure HALOFIT [96] to calculate the non-linear power spectrum.

2. The Weak Lensing 2 function

For the weak lensing spectrum, the uncertainty is given by: [91, 93]

$$P_1 = \frac{s}{\frac{2}{(2l+1)f_{\text{sky}}} P_1 + \frac{\text{int}^2}{n}} ; \quad (28)$$

where $f_{\text{sky}} = 129600$ is the fraction of the sky covered by a survey of dimension in degrees, and $\text{int}^2 = 0.4$ is the intrinsic ellipticity of galaxies. We consider a reference survey with $f_{\text{sky}} = 0.7$, in the same range as the Pan-STARRS survey [97]. We used an average galaxy number density of $n = 6.6 \cdot 10 \text{ sr}^{-1}$. 2 was computed between multipoles l_{min} and l_{max} . For l_{min} , we took the fundamental mode approximation:

$$l_{\text{min}} \cdot \frac{360 \text{ deg}}{r} = \frac{r}{f_{\text{sky}}} ; \quad (29)$$

i.e. we considered only lensing modes for which at least one wavelength can fit inside the survey area. We used $l_{\text{max}} = 3000$, since on smaller scales the nonlinear approximation HALOFIT to the nonlinear power spectrum may not be valid.

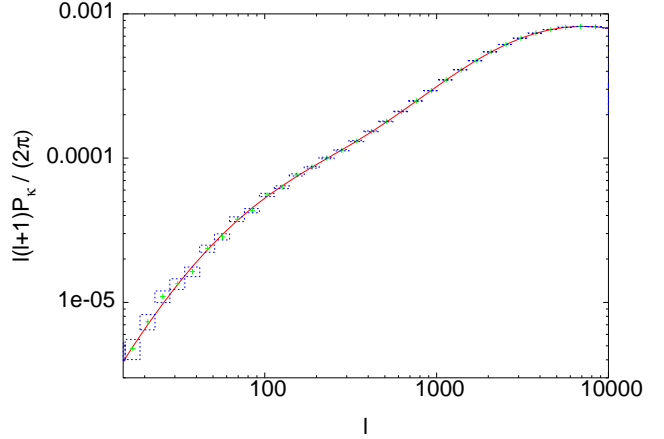


FIG. 10: Monte-Carlo simulated convergence power spectrum. The points with error boxes are the simulated "data" for a survey with $f_{\text{sky}} = 0.7$, $n = 6.6 \cdot 10 \text{ sr}^{-1}$ and $\text{int}^2 = 0.4$, while the solid line is the fiducial model.

3. Simulation

The procedure described above was used to generate fiducial convergence power spectra $P_1^{(f \text{ id})}$. We used the cosmological parameter fiducial values of Sec. IIIA. We then calculated the uncertainties on the convergence power spectra using Eq. (28). The Monte-Carlo simulated convergence power spectra are generated using

$$P_1^{\text{MC}} = P_1^{(f \text{ id})} + r P_1 \quad (30)$$

where r is randomly chosen from a Gaussian distribution of standard deviation 1 [58]. The simulated convergence power spectrum for the reference survey and the fiducial model are shown in Fig. 10.

IV. RESULTS AND DISCUSSION

A. Goals

As we have said, the most important question in the study of dark energy today is whether the dark energy is or is not a cosmological constant. If dark energy is shown not to be a cosmological constant, the next questions that arise are again qualitative: Is the equation of state greater or less than -1? Does it vary with time? The actual values of $w(0)$ and $w'(0)$ will become important in the more distant future, when theoretical models for the form of $w(z)$ are available. We look for constraints on the equation of state parameters, not because we believe that any one of the parametrizations (1, 2, 3, 4) is a theoretically favored model for $w(z)$, but because we wish to address the above qualitative questions about dark energy. Thus, we emphasize that our goal is to answer these qualitative questions in a careful, parametrization-

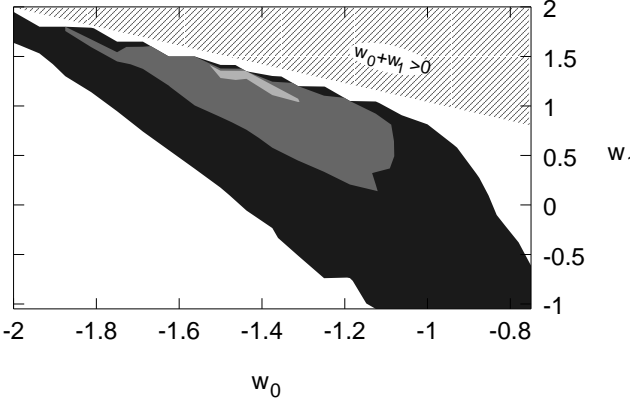


FIG. 11: Current constraints on dynamical dark energy parametrized by (4), using first-year WMAP data, the SNe Ia ‘gold set’ from [11], and the current SDSS data. The 1 contour (light gray), the 2 contour (dark gray), and the 3 contour (black) are shown. The region of parameter space excluded by the $w_0 + w_1 > 0$ prior is filled with upwards-sloping stripes.

independent way, rather than to find specific values for $w(0)$ and $w^0(0)$ within a particular parametrization.

B. Analysis of Current Data

Keeping these goals in mind, we used χ^2 minimization to analyze current data from the CMB power spectrum [12], the SNe Ia ‘gold set’ [11], and the galaxy power spectrum [15]. We began by using (4) to parametrize the dark energy equation of state. The contours obtained are plotted in Fig. 11, with grid spacings $w_0 = 0.06$ and $w_1 = 0.15$. The resulting 1 and 2 constraints on the dark energy parameters are $w_0 = 1.38^{+0.08+0.30}_{-0.20-0.55}$ and $w_1 = 1.2^{+0.40+0.64}_{-0.16-1.06}$, with a best-fit χ^2 value of 1611. We consider our 2 contours to be more reliable than our 1 contours, since the latter occupy an area in Fig. 11 only a few times the area of a grid square.

CDM models are not conclusively ruled out by our results. Compared to the best-fit model in Fig. 11, the CDM model has a χ^2 value that is higher by 5. However, the cosmological constant is a ‘‘simpler’’ model of dark energy than the $w(z)$ parametrizations considered here, in the sense that the CDM model has two fewer variable parameters than (1, 2, 4). Thus the CDM model has $\chi^2_{\text{d.o.f.}} = 1616 - 1514 = 1.0676$, while the best-fit model from Fig. 11 has $\chi^2_{\text{d.o.f.}} = 1611 - 1512 = 1.0656$. In the approximation that uncertainties in the data points are Gaussian, these correspond to probabilities of $P_{\text{CDM}} = 0.0336$ and $P_{\text{best fit}} = 0.0378$. For comparison, a point on the edge of the 2 contour in Fig. 11 has $\chi^2_{\text{d.o.f.}} = 1615 - 1512 = 1.0682$ and probability 0.0324. In this sense, the CDM model is more probable than some points within the 2 contour. Although the data favor $w_0 < -1$ and $w_1 > 0$, the cosmological constant is not decisively ruled out as a model of dark

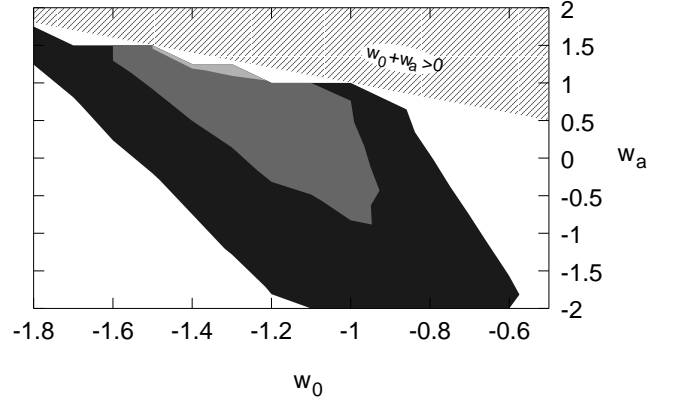


FIG. 12: Same as Fig. 11, except that the dark energy parametrization (2) has been used. The region of parameter space excluded by the $w_0 + w_a > 0$ prior is filled with upwards-sloping stripes.

energy.

It is troubling that the best-fit model in Fig. 11 is so close to the boundary $w_0 + w_1 = 0$ of the dark energy parameter space. This is despite the fact that (4), out of the three 2-parameter equations of state illustrated in Fig. 1, covers the greatest range of parameters in the $(z, w(z))$ plane. Parametrization (2), widely used in the literature, is more restrictive than (4), and therefore should have more problems with this boundary. We repeated our analysis using (2), obtaining the χ^2 contours shown in Fig. 12 with grid spacings $w_0 = 0.1$ and $w_a = 0.25$. The resulting 2 bounds are $w_0 = 1.3^{+0.39}_{-0.34}$ and $w_a = 1.25^{+0.40}_{-2.17}$, with a best-fit χ^2 value of 1613. Thus we see that the allowed region shifts significantly when we switch to parametrization (2), with $w^0(0) < 0$ models falling within the 2 contours. Also, the minimum χ^2 value goes up by 1.8.

These shifts are better understood when the χ^2 functions corresponding to the two parametrizations are plotted together in the (w_0, w^0) plane (with $w^0 = w(1) - w(0)$), as in Fig. 13. Note, first of all, that the two sets of χ^2 contours would be nearly identical if the region of parameter space between the dotted lines were removed. This region corresponds to the slice of the $(z, w(z))$ plane between the dashed and solid lines in Fig. 1, which is allowed by parametrization (4) but not by (2). Also note that the best-fitting point ($w_0 = 1.38, w^0 = 1.2$) of parametrization (4), marked by an ‘‘X’’ on the plot, is simply outside the range allowed by parametrization (2). Since the minimum χ^2 found using (2) is higher, the 2 contour is at a higher χ^2 , meaning that it now encloses some points with $w_a < 0$. Thus, the difference between the constraints found using (4) and (2) is directly related to the parametrization, and particularly, to the high redshift $w(z)$ constraint discussed in Sec. II A.

To summarize, switching parametrizations from (4) to (2) moves the boundary downwards, pushing the contours in the direction of decreasing w^0 . Since the contours

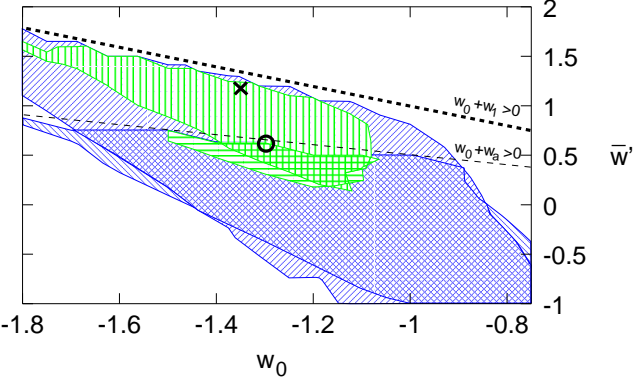


FIG. 13: Comparison of the two dark energy parametrizations (2, 4). Contours corresponding to (4) are filled with vertical stripes ($\chi^2 = 1615$ contour) or upwards-sloping stripes ($\chi^2 = 1620$ contour), and the best-fit model is marked by an 'X'. Contours corresponding to (2) are filled with horizontal stripes ($\chi^2 = 1615$ contour) or downwards-sloping stripes ($\chi^2 = 1620$ contour), and the best-fit model is marked by an 'O'. Note that the $\chi^2 = 1615$ and $\chi^2 = 1620$ contours are the 2 and 3 contours, respectively, of parametrization (4). The thick and thin dashed lines correspond to the lines $w_0 + w_1 = 0$ and $w_0 + w_a = 0$, respectively.

in Fig. 11 are still near the boundary, a parametrization that allows larger values of w^0 may allow the contours to shift even more in that direction. It is possible that such a parametrization would favor $w_0 < -1$ and $w^0 > 0$ to an even larger degree, leaving the CDM model less favored.

Comparison with the published literature shows that our results are consistent with others obtained using various combinations of cosmological probes. Table V lists several recent analyses, along with the parameters and $w(z)$ parametrizations used (parameters w^0 , w_a , and w_1 imply parametrizations (1), (2), and (4), respectively), the priors, and the resulting $w(z)$ constraints. When $w(z)$ constraints using the same equation of state parametrizations are compared, our results are consistent with those in Table V at the 2 level. In addition, the results of [11, 99], obtained using parametrization (1) and SN Ia data, are consistent with our constraints using either of the parametrizations (2, 4). It is reassuring that our χ^2 minimization procedure, which handles parameter degeneracies differently than marginalization, obtains consistent results.

Several papers list constraints on $w(z)$ at specific values of z , as shown in Table VI. It is evident from the table that $w(0:3)$ is well-constrained and parametrization-independent. Our results for $w(0:3)$ are in excellent agreement with those of [52], even when their three-parameter equation of state (3) is used. Meanwhile, the equation of state at $z = 1$ is less well constrained, though once again our results agree with those of [52] at the 2 level. Parametrization (4) evidently prefers higher values of $w(1)$ than does (2). One would ex-

pect the addition of the third parameter in (3) to bridge the gap between constraints using (2) and (4). However, our best-fit models using (4) have $w(0) = 1.4$, $w(0:3) = 1$, and $w(1) = 0.2$. Even 3X cannot reproduce all three of these features if one also imposes the CMB constraint $w(z) = 0$ at $z = 1$, which implies $w_0 + w_a + w_b = 0$. That is, setting $w(0) = -1.38$ and $w(1) = -0.18$ from our best-fit model, and imposing the requirement that $\lim_{z \rightarrow 1} w(z) = 0$, implies that $w(0:3) = 0.70$ in parametrization (3), which is inconsistent with constraints on $w(0:3)$ discussed above. Since our best-fit models are qualitatively different from those allowed using the parametrizations (2) and (3), there is still no discrepancy between our results and those of [52] for $w(1:0)$. Finally, recall that the two-parameter equations of state (1, 2, 4) relate $w(z)$ and its derivative, at low redshifts, to the equation of state in the large redshift limit (see Table I). Our constraints on the large redshift value of the equation of state, $\lim_{z \rightarrow 1} w(z)$, agree closely with those of [102]. These results appear to be independent of parametrization; analyses with three different parametrizations agree that $w(z)$ at large redshifts is slightly less than zero.

Our uncertainties in the dark energy parameters are mostly in agreement with similar analyses that include CMB and SN Ia data. Our 2 uncertainties in w_0 and $w_0 + w_a = \lim_{z \rightarrow 1} w(z)$ are approximately twice as large as the 68.3% constraints of [102], just as expected. Also, our 2 constraints on w_0 are about twice as large as the 1 uncertainties of [98]. Their looser bounds on $w^0(0)$ can be attributed to the fact that they use a four-parameter equation of state, and marginalize over parameters other than those reported. Meanwhile, comparison of our results with [52] provides an example of parametrization effects on the dark energy constraints. Their 95.5% upper and lower bounds on w_0 are nearly the same as our 2 bounds, and their 95.5% lower bound on w_a is somewhat tighter than ours. However, our upper bound on w_a is smaller than theirs by a factor of three, due to the fact that our best-fit model is much nearer to the boundary $w_0 + w_a = 0$ of parameter space. Still, the boundary has some effect on their 95.5%, and 99.86% probability bounds on w_a . Although their 68.3% upper and lower bounds are nearly the same, their 99.86% upper bound is smaller than the lower bound by a factor of two. Thus, it would be interesting to see their analysis repeated with parametrization (4), which has a less restrictive boundary.

The effects of systematic uncertainties can be estimated by comparing the analysis procedures used by the studies listed Table V, as well as the locations of the resulting contours in parameter space. Ref. [52] finds 68% and 95% contours centered near the CDM model, while [11, 98, 100, 101, 102] as well as our analysis find contours that lie mostly in the $w_0 < -1$, $w^0(0) > 0$ region. Even when the analysis of [52] is repeated without the Lyman and galaxy bias data sets, their preferred models are still close to the CDM model [103]. Since both studies use the standard SN Ia likelihood, the difference between

Ref.	probes included	parameters varied	priors	dark energy constraints
[11]	SN Ia	w_0, w^0, Ω_m	$\Omega_m = 0.27 \pm 0.04$	$w_0 = 1.31^{+0.22}_{-0.28},$ $w^0 = 1.48^{+0.81}_{-0.90}$
[52]	CM B, SN Ia, P(k), bias, Ly-	\textit{vanilla"}, w_0, w_a	< 0.3	$w_0 = 0.98^{+0.193+0.384+0.568}_{-0.193-0.373-0.521},$ $w_a = 0.05^{+0.65+1.13+1.38}_{-0.83-1.92-2.88}$
[98]	CM B, SN Ia, P(k)	\textit{vanilla"}, 4 w(z) parameters	$h = 0.72 \pm 0.08, 0 < \Omega_m < 1,$ $0.014 < \Omega_b < 0.04, 0 < \Omega_a < 1,$ $0.6 < n_s < 1.4$	$w_0 = 1.43^{+0.16}_{-0.38},$ $\frac{dw}{dz} = 1.0^{+1.0}_{-0.8} \Big _{z=0}$
[99]	SN Ia	w_0, w^0, Ω_m	$d_{AC}^{(dec)} \Big _{\Omega_m=0.27} = 1.716 \pm 0.062,$ $\frac{d \ln D}{d \ln a} \Big _{z=0.15} = 0.51 \pm 0.11$	$1.05 < w_0 < 0.29,$ $1.89 < w^0 < 0.05^a$
[99]	SN Ia	w_0, w^0, Ω_m	$\Omega_m = 0.27 \pm 0.04$	$1.39 < w_0 < 0.25,$ $2.61 < w^0 < 1.49^a$
[100]	SN Ia	$\Omega_m, 3 w(z)$ parameters	$d_{AC}^{(dec)} \Big _{\Omega_m=0.27} = 1.710 \pm 0.137,$ $\Omega_b = 0.024, \Omega_m = 0.14 \pm 0.02$	$w_0 \Big _{0 < z < 0.414} = 1.287^{+0.016}_{-0.056},$ $w_0 \Big _{0.414 < z < 1} = 0.229^{+0.070}_{-0.117},$ $w_0 \Big _{z < 1.755} = 0.142^{+0.051}_{-0.033}$
[101]	SN Ia	w_0, w_a	$\Omega_m = 0.27$	$w_0 = 1.38 \pm 0.21,$ $w_a = 2.78 \pm 1.32$
[101]	SN Ia	w_0, w_a	$\Omega_m = 0.31$	$w_0 = 1.35 \pm 0.24,$ $w_a = 2.32 \pm 1.56$
[101]	SN Ia	w_0, w_a	$\Omega_m = 0.35$	$w_0 = 1.3 \pm 0.29,$ $w_a = 1.64 \pm 1.95$
[102]	CM B, SN Ia, X-ray	\textit{vanilla"}, bias, w_0, w_a	$\text{bias} = 0.824 \pm 0.089,$ $\Omega_b = 0.0214 \pm 0.0020,$ $h = 0.72 \pm 0.08$	$w_0 = 1.16^{+0.22}_{-0.19},$ $w_0 + w_a = 0.05^{+0.09}_{-0.17}$
[102]	CM B, SN Ia, X-ray	\textit{vanilla"}, bias, Ω_m, w_0, w_a	$\text{bias} = 0.824 \pm 0.089,$ $\Omega_b = 0.0214 \pm 0.0020,$ $h = 0.72 \pm 0.08$	$w_0 = 1.14^{+0.31}_{-0.21},$ $w_0 + w_a = 0.09^{+0.12}_{-0.16}$
[102]	CM B, SN Ia, X-ray	\textit{vanilla"}, bias, 3 w(z) parameters	$\text{bias} = 0.824 \pm 0.089,$ $\Omega_b = 0.0214 \pm 0.0020,$ $h = 0.72 \pm 0.08$	$w_0 = 1.23^{+0.34}_{-0.46},$ $\lim_{z \rightarrow 1} w(z) = 0.12^{+0.11}_{-0.76}$
AU, M I, PJS	CM B, SN Ia, P(k)	\textit{vanilla"}, w_0, w_1	for priors see Table II	$w_0 = 1.38^{+0.30}_{-0.55},$ $w_1 = 1.2^{+0.64}_{-1.06}$ (2 constraints)
AU, M I, PJS	CM B, SN Ia, P(k)	\textit{vanilla"}, w_0, w_a	for priors see Table II	$w_0 = 1.3^{+0.39}_{-0.34},$ $w_a = 1.25^{+0.40}_{-2.17}$ (2 constraints)

^aBounds taken from plot of 68% probability contour

TABLE V : Dynamical dark energy constraints from current data. The \textit{vanilla} parameter space is spanned by the six parameters ($h, \Omega_m, \Omega_b, A, n_s$). The cosmological probes used are: bias = SDSS galaxy bias, CM B = WMAP CM B power spectra, Ly- = SDSS Lyman- α , P(k) = SDSS galaxy power spectrum, SN Ia = SN Ia \textit{gold set"}, X-ray = Chandra X-ray clusters.

their result and ours must come from either their CM B likelihood function [104] or their galaxy power spectrum analysis [52, 105]. Ref. [104] claims that the WMAP likelihood approximation is inaccurate at low l , and that the WMAP foreground removal procedure may lead to a suppression of low- l power. Their likelihood function is designed to correct these problems. Meanwhile, their galaxy power spectrum analysis uses SDSS measurements up to $k = 0.2 \text{ h/Mpc}$, a range which extends into the non-linear regime. The combined effect of these two changes is to move the contours very close to the CDM model, which is disfavored by $\chi^2 = 3$ in our analysis with the same w(z) parameterization. Thus, differences in the CM B and galaxy power spectrum likelihood functions lead to a shift of over 1 in the χ^2 contours.

We attempted to reproduce this shift by using only the multipoles $l \leq 20$ in our CM B analysis. If the low multipoles were responsible for the shift, then neglecting them would enlarge the χ^2 contours and move them towards the CDM model. However, as shown in the third column of Table V II, the allowed region actually moves away from that of [52], although it does broaden somewhat. Not only does this test fail to explain the difference between the regions of parameter space preferred by [52] and our results, it also demonstrates that the CM B analysis is sensitive to the low l region of the power spectrum. Since there is an ongoing debate about the proper handling of the low multipoles [104], this sensitivity to that region of the power spectrum is worrisome.

Recall that switching dark energy parameterizations

z	Ref.	Parametrization	w(z) constraint
0.3	[52]	(2)	$1.01^{+0.176}_{-0.215}$ (95.5%)
	[52]	(3)	$0.98^{+0.205}_{-0.249}$ (95.5%)
	AU, M I, PJS	(4)	$1.02^{+0.118}_{-0.33}$ (2)
	AU, M I, PJS	(2)	$1.01^{+0.119}_{-0.29}$ (2)
1	[52]	(2)	$1.00^{+0.27}_{-0.66}$ (95.5%)
	[52]	(3)	$1.03^{+0.39}_{-0.58}$ (95.5%)
	AU, M I, PJS	(4)	$0.18^{+0.12}_{-0.80}$ (2)
	AU, M I, PJS	(2)	$0.68^{+0.08}_{-0.74}$ (2)
1	[102]	(2)	$0.05^{+0.09}_{-1.17}$
	[102]	3 w(z) param.s.	$0.12^{+0.11}_{-0.76}$
	AU, M I, PJS	(4)	$0.18^{+0.12}_{-0.80}$ (2)
	AU, M I, PJS	(2)	$0.05^{+0.05}_{-1.78}$ (2)

TABLE VI: Constraints on w(z) at several redshifts.

Analysis	Param.	w_0 (to 2)	w_1 or w_a (to 2)
standard	(4)	$1.38^{+0.30}_{-0.55}$	$w_1 = 1.2^{+0.64}_{-1.06}$
standard	(2)	$1.3^{+0.39}_{-0.34}$	$w_a = 1.25^{+0.40}_{-2.17}$
CMB 1 20	(4)	$1.63^{+0.43}_{-0.65}$	$w_1 = 1.5^{+0.45}_{-1.67}$
$w_0 + 2w_1 = 0$	(4)	$1.25^{+0.40}_{-0.38}$	$w_1 = 0.6^{+0.23}_{-1.4}$, $w_a = 2w^0 = 1.2^{+0.46}_{-2.8}$
CMB 1 20			

TABLE V II: Consistency checks of our current w(z) constraints. All constraints shown are at the 2 level. The "standard" analyses above use WMAP, SDSS, and SN Ia gold set data, with priors as shown in Table II.

can change the uncertainties in $w(0)$ and $w^0(0)$. In order to test the effects of this parametrization dependence in combination with the low 1 sensitivity, we imposed the prior constraint $w_0 + 2w_1 = w_0 + 2w^0 = 0$ on the analysis with CMB 1 20. This allowed us to estimate the constraint on w_a that we would have obtained if we had repeated the analysis with parametrization (2). The resulting 2 constraints, shown in the fourth row of Table V II, are very similar to those found by the standard analysis using parametrization (2). They have not moved appreciably towards the CDM model, though the uncertainties have grown. The slight shift away from CDM seen without the prior $w_0 + 2w^0 = 0$ has been hidden by the imposition of that prior. This implies that the parametrization dependence of the results conceals some of their sensitivity to low 1 CMB data. Once again, we are unable to reproduce the shift in the location of the equation of state contours. The explanation may have to do with the details of the CMB likelihood function used by [52], or with their galaxy power spectrum analysis. These differences between the likelihood functions should be examined critically.

Similarly, the SN Ia likelihood function used by [99] causes the dark energy constraints to shift relative to those in [11]. The standard supernova analysis [11] predicts $1.59 < w_0 < 1.09$ and $0.58 < w^0 < 2.29$. Using the same dark energy parametrization and the same prior $w_m = 0.27 \pm 0.04$, [99] obtains $1.39 < w_0 < 0.25$ and

$2.61 < w^0 < 1.49$. The [99] analysis uses supernova averaging [106] to handle systematic effects due to the weak lensing of supernovae [107]. The averaging method assumes that uncertainties in SN Ia fluxes, rather than in magnitudes, are Gaussian. If uncertainties are actually Gaussian in magnitude, this introduces a bias [106]; conversely, if uncertainties are Gaussian in flux, then the standard SN Ia analysis is biased. The net effect of the flux averaged likelihood function is to weaken constraints on w_0 and w^0 , and to shift them both by about 1 towards the CDM model.

Another SN Ia systematic effect, not included in any of the analyses in Table V, is the dimming of supernovae by astrophysical dust. Ref. [108] considers several types of intergalactic dust, and constrains supernova dust dimming to be less than 0.2 magnitudes. (For an extensive discussion of SN Ia systematics and their effects on the cosmological parameters, see [72].) The upper bound on dust dimming is not much less than the mean SN Ia magnitude uncertainty in the current data set, which suggests that dust dimming can cause a significant bias in dark energy constraints. Since the dimming of SNe Ia provides evidence for accelerating cosmological expansion, additional dimming due to dust will appear to exaggerate this acceleration. Ignoring systematic uncertainties due to dust dimming will cause an analysis to underestimate w , since more negative values of the equation of state lead to a more rapid acceleration.

To summarize, current data are not precise enough to address whether or not the dark energy is a cosmological constant. A careful study of the current data, and comparisons with other recent analyses, reveals several obstacles to a satisfactory understanding of the dark energy. The degeneracy between w_0 and w_1 remains unresolved, and the allowed 2 ranges for w_0 and w_1 are at least

$1.93 < w_0 < 1.08$ and $0.14 < w_1 < 1.84$. Furthermore, this result is dependent on the parametrization chosen for the dark energy equation of state. In particular, problems arise when the 1 and 2 contours lie near a boundary of the dark energy parameter space, as they do at present. More generally, uncertainties in the equation of state parameters depends on the location of the best-fit model in the parameter space. Aside from the parametrization dependence issues, analyses that use the same data, but different treatments of the systematics, and best-fit models differing by 1. The combination of parametrization dependence and systematic effects is enough to shift the best-fit model by more than 2. Thus we cannot rule out the CDM model at present.

C. Forecasts using Simulated Data

Next we ask, when data from future probes are available, how close we can come to achieving our goal of distinguishing between a cosmological constant and other forms of dark energy. The dark energy parameter space is continuous, with nonconstant $w(z)$ models arbitrarily

close to the CDM model. Unless we are lucky and find a dark energy significantly different from the cosmological constant, the best we can do is to distinguish between models separated by some minimum distance in parameter space.

Thus, we begin by identifying a pair of reasonable milestones against which progress in $w(z)$ constraints may be measured. Since we do not know ahead of time which best-fit model will be found, we will say that an experiment can distinguish between two points A and B in parameter space if, regardless of the location of the best-fit model, the 2 σ contour around that best-fit model excludes either A or B (or both).

Our first milestone is to distinguish between the CDM model and tracker quintessence [109] or tracker SUGRA [110] models with $w_0 > 0.8, w_1 > 0$. These are interesting, partly because they represent a large class of well-established, theoretically motivated models, and also because they make definite predictions that are clearly distinct from the CDM model in parameter space. It is not clear whether such models are ruled out by current data; our analyses exclude them to greater than 2 σ , but they are within the 95% probability contour of [52]. In the future, we can compare an arbitrary best-fit model to CDM and tracker models by comparing their values of $w(0.3)$. The CDM model predicts $w(0.3) = 1$, while trackers have $w(0.3) > 0.8$. In the worst case, the future best-fit model will have $w(0.3) = 0.9$. Therefore, in order to reach the first milestone, we must reduce the 2 σ uncertainty in $w(0.3)$ to about 0.1.

As our second milestone, we would like to distinguish between CDM and quintessence models that are near to it. We do not have in mind any particular class of theoretical models, so "near" is not well-defined. As a reasonable second milestone, we consider aiming to distinguish CDM from models with either $|w_0 + 1| > 0.05$ and $w_1 = 0$, or $w_0 = -1$ and $|w_1| > 0.05$. For this we will need both $w_0(2) < 0.025$ and $w_1(2) < 0.025$, that is, $w_0 = w_1 = 0.01$. If the CDM model were to be the preferred model even when the equation of state uncertainties were reduced to this level, then it would probably be time to abandon our hopes of using $w(z)$ to study the nature of dark energy.

Now that Sec. IV B has pointed out several pitfalls in the analyses of current data, we make the reasonably optimistic assumption that the likelihood functions associated with the CMB, SNe Ia, and cosmic shear will be well understood by the end of the decade. We assume that these new, accurate likelihood functions will give no less cosmological information than the likelihood functions discussed in Sections IIIB, IIIC, and IIID. This assumption is optimistic; the conservative CMB foreground removal procedure of [104], as well as the inclusion of SN Ia dust damping effects, should increase uncertainties in the dark energy parameters. Moreover, for weak lensing, several systematic effects (e.g. intrinsic alignments of source galaxies, selection biases and residuals from the PSF correction) need to be better understood and tightly

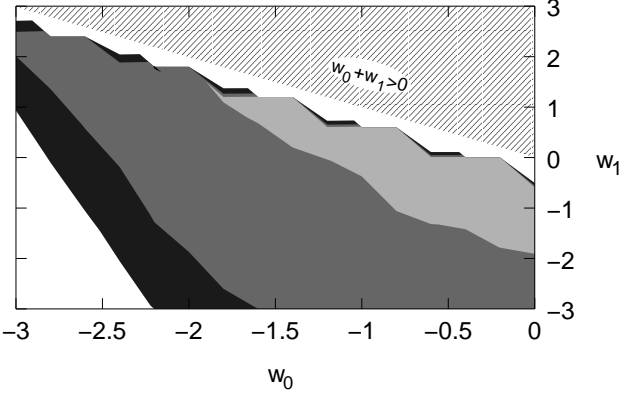


FIG. 14: Forecast CMB constraints on dark energy. The 1 σ contour (light gray), the 2 σ contour (dark gray), and the 3 σ contour (black) are shown.

controlled in order for this probe to achieve its full potential [111].

Also, our forecasts are based on a CDM fiducial model, since $(w_0 = -1, w^0(0) = 0)$ is far from both the parameter space boundaries $w_0 + w_1 = 0$ and $w_0 + w_a = 0$. From now on, we limit our study to the parameterization (4) alone. Assuming that our 2 σ contours stay away from the boundaries, we can compare constraints between parameterizations (4) and (2) using the "rule of thumb" $w_1 = w^0 - w_a = 2$, where the average low redshift derivative $w^0 = w(1) - w(0)$. The factor of 1=2 means that, even when parameter space boundaries are unimportant, the uncertainty in the derivative $w^0(0)$ is parameterization dependent.

Dark energy constraints provided by eight years of simulated WMAP data alone are shown in Fig. 14, with grid spacings $w_0 = 0.3$ and $w_1 = 0.6$. Models in the upper right-hand section of Fig. 14 are ruled out by the prior constraint $w_0 + w_1 < 0$. Meanwhile, the requirement that $h < 1.1$ eliminates models in the lower left-hand corner of the plot. Therefore, to 2 σ , virtually no constraints are imposed on w_0 and w_1 within the ranges shown in Fig. 14. Such weak CMB constraints on dynamical dark energy are to be expected, given the angular diameter distance degeneracy discussed in Sec. II B.

Given the fairly weak priors used here, the supernovae alone were also unable to provide interesting constraints on dynamical dark energy. An analysis of the supernova dataset shown in Fig. 6 gave deceptively tight constraints on w_1 ; see Fig. 15, with grid spacings $w_0 = 0.008$ and $w_1 = 0.04$. However, multiple Monte Carlo simulations of SN Ia datasets yielded 2 σ constraints that varied widely from simulation to simulation. Three out of our five simulations had 2 σ contours extending into the $w_1 < -5$ range.

The problem, as pointed out in [112], is that the dark energy density $\rho_{\text{de}}(z)$ exhibits qualitatively very different behaviors for $w_1 > 0$ and $w_1 < 0$. When $w_1 > 0$, $\rho_{\text{de}}(z)$ can remain a nontrivial fraction of the total energy den-

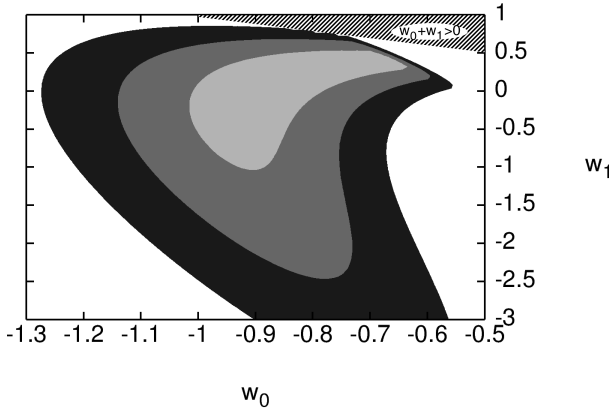


FIG. 15: SN Ia contours for the simulated dataset shown in Fig. 6. The 1 contour (light gray), the 2 contour (dark gray), and the 3 contour (black) are shown.

sity of the universe up to red shifts of order unity. When $w_1 < 0$, $w_{de}(z)$ drops quickly with increasing red shift, so that the dark energy is important only in the very recent past. Distinguishing between different dark energy models is difficult when $w_{de}(z)$ is very small. This explains the fact that several of the simulated 2 contours extend deep into the $w_1 < 0$ region even though they are all simulations of a model with $w_1 = 0$.

Adopting strong priors on Ω_m significantly reduces these non-Gaussianities, as shown in Fig. 16 (top). When we fix $\Omega_m = 0.31$ and repeat the analysis of five simulated data sets, we find mean 2 uncertainties on w_0 and w_1 of $w_0(2) = 0.182$ and $w_1(2) = 0.687$. The standard deviations in $w_0(2)$ and $w_1(2)$ are 0.0037 and 0.031, respectively. Thus when Ω_m is fixed, the uncertainties vary by only a few percent from one simulation to another.

However, [113] points out the perils of assuming strong priors in the SN Ia analysis. In particular, if the analysis of another cosmological probe is based on the assumption that $w(z) = -1$, then the constraints from that analysis should not be imposed as priors in a study of dynamical dark energy. Figs. 16 (mid) and 16 (bot) show the effects of weakening the prior constraint on Ω_m to $\Omega_m = 0.31 \pm 0.05$ and $\Omega_m = 0.31 \pm 0.10$, respectively. Even with the relatively strong priors used in Fig. 16 (mid), the non-Gaussianities have returned, and constraints on the dark energy parameters are weakened. Thus it is imperative that the supernovae be combined with another data set in order to provide constraints on dynamical dark energy.

Combination of the WMAP-8 and SN Ia datasets improved dark energy constraints considerably, as shown in Fig. 17, with grid spacings $w_0 = 0.04$ and $w_1 = 0.2$. We obtained the 1 constraints $w_0 = 0.09$ and $w_1 = 0.33$, and the 2 constraints $w_0(2) = 0.19$ and $w_1(2) = 0.68$. The 2 uncertainty in $w(z)$ at $z = 0.3$ was found to be $w(0.3)(2) = 0.12$. We checked these using a Fisher matrix calculation and found the 1 con-

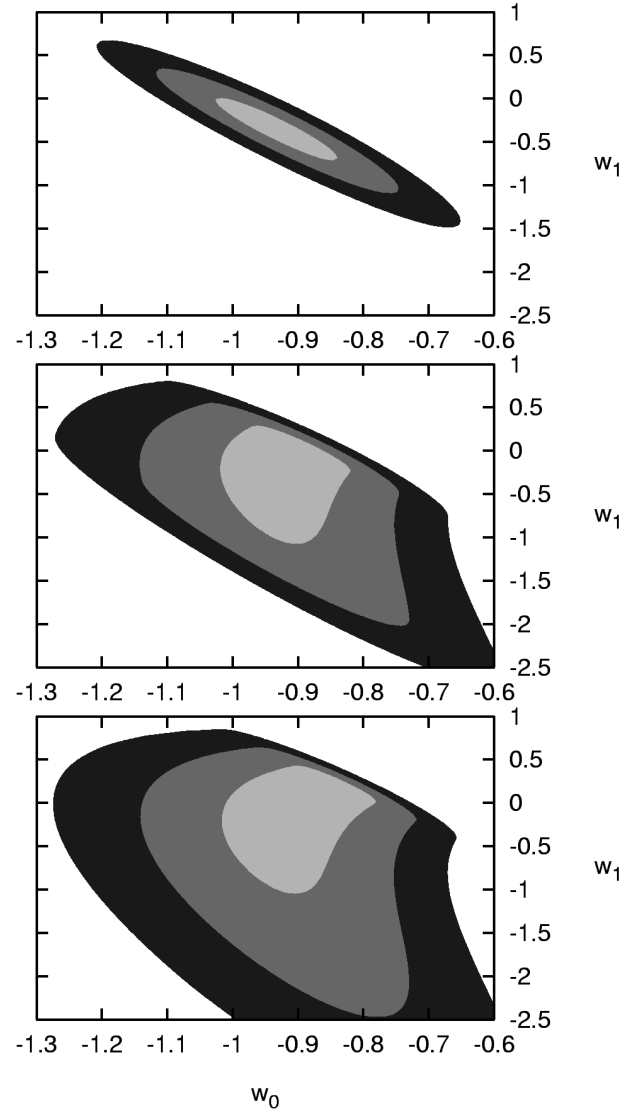


FIG. 16: SN Ia contours for the simulated dataset shown in Fig. 6, assuming the prior constraints $\Omega_m = 0.31$ (top), $\Omega_m = 0.31 \pm 0.05$ (mid), and $\Omega_m = 0.31 \pm 0.10$ (bot). The 1 contour (light gray), the 2 contour (dark gray), and the 3 contour (black) are shown.

straints $w_0 = 0.08$ and $w_1 = 0.30$, consistent with our minimization results. Our results correspond closely with those of [38] with SNe Ia and a prior on Ω_m , as shown in the first row of Table V III.

As with the supernova analysis, four additional simulated datasets were analyzed separately. The 2 contours for the five sets all have approximately the same areas and degeneracy directions. From these five simulations, the mean 2 uncertainties on w_0 and w_1 were 0.20 and 0.73, respectively, and the standard deviations in the 2 uncertainties were 0.018 and 0.071, respectively. This implies that our forecast uncertainties are each correct to about 10%. Since the main CMB + SN Ia analysis used

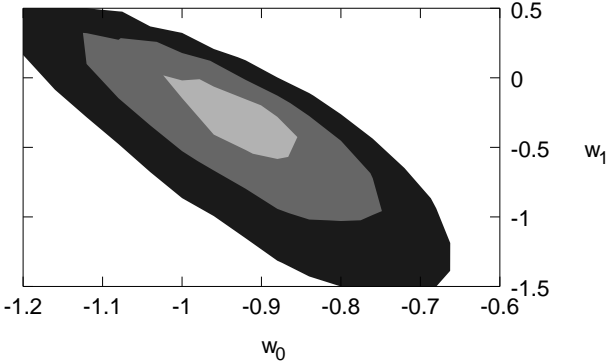


FIG. 17: Forecast CM B and SN Ia constraints on dark energy. The 1 σ contour (light gray), the 2 σ contour (dark gray), and the 3 σ contour (black) are shown.

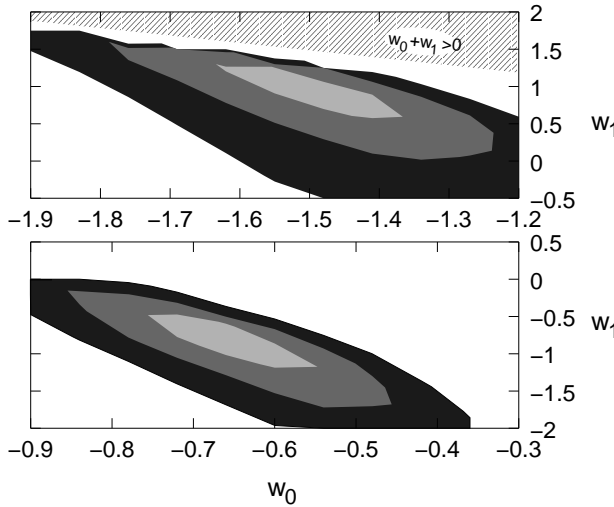


FIG. 18: χ^2 contours for CM B and SN Ia "data" simulated using the fiducial models ($w_0 = -1.3, w_1 = 0.5$) (top) and ($w_0 = -0.7, w_1 = 0.3$) (bottom). The 1 σ contours (light gray), 2 σ contours (dark gray), and 3 σ contours (black) are shown.

a finer grid than the others, allowing the determination of 1 as well as 2 constraints, we have reported the constraints from that set alone. Nevertheless, it is reassuring that this set is consistent with the other simulations.

Next, the analysis was repeated with two different fiducial models, chosen to lie approximately along the line of degeneracy in the (w_0, w_1) plane. As shown in Fig. 18, the model ($w_0 = -1.3, w_1 = 0.5$) had 2 uncertainties of 0.26 and 0.85 on w_0 and w_1 , respectively, while the model ($w_0 = -0.7, w_1 = 0.3$) had uncertainties of 0.20 and 0.77. These are consistent with our constraints obtained using the CDM fiducial model.

Returning to our CDM fiducial model, we repeated the analysis with different assumptions about the data in order to test the robustness of our forecast constraints.

Ref.	surveys included	parameters varied; priors	forecast constraints
[36]	Planck + W L (1000 deg 2)	\textit{"vanilla"}, $w_0, T=S$; $w^0 = 0$	$w_0 = 0.15$
[37]	W L + COBE + photo z + Planck	$!_m, !_b, n_s, m, w_0$; $w^0 = 0$, $\ln !_m = .064$, $\ln !_b = .035$, $n = .04$, $m = .58$	$w_0 = 0.19$
[38]	SNAP SNe Ia	w_0, w_a, m ; $m = 0.03$, $K = 0$	$w_0 = 0.09$; $w^0 = 0.31$
[38]	SNAP SNe Ia	w_0, w_a, m ; Planck priors, $K = 0$	$w_0 = 0.09$; $w^0 = 0.19$
[38]	SNAP SNe Ia + W L	w_0, w_a, m ; $K = 0$	$w_0 = 0.05$; $w^0 = 0.11$
[39]	Planck + W L ($f_{\text{sky}} = 1$, tomography)	\textit{"vanilla"}, $w_0, w_a, !, s, Y_{\text{He}}$	$w_0 = 0.056$, $w_a = 0.087$
[39]	Planck + W L ($f_{\text{sky}} = 0.5$, tomography)	\textit{"vanilla"}, $w_0, w_a, !, s, Y_{\text{He}}$	$w_0 = 0.076$, $w_a = 0.11$
[39]	4 yr. WMAP + W L ($f_{\text{sky}} = 1$, tomography)	\textit{"vanilla"}, $w_0, w_a, !, s, Y_{\text{He}}$	$w_0 = 0.064$, $w_a = 0.11$
[40]	Planck + SNAP SNe Ia + W L ($f_{\text{sky}} = 0.5$, tomography)	\textit{"vanilla"}, $w_0, w_a, !, s, Y_{\text{He}}$	$w_0 = 0.05$, $w_a = 0.1$
[41]	Planck + LSST cluster counts and power spectrum (400,000 clusters)	$!_b, !_m, \text{de}, 8, n_s, w_0, w_a$; linear biasing	$w_0 = 0.014$, $w_a = 0.049$
[41]	Planck + LSST cluster counts and power spectrum (60,000 clusters)	$!_b, !_m, \text{de}, 8, n_s, w_0, w_a$; linear biasing, $M_{\text{min}} = 2 \cdot 10^4 h^{-1} M_{\odot}$	$w_0 = 0.026$, $w_a = 0.090$
AU, MI, PJS	8 yr. WMAP + 2200 SNe	\textit{"vanilla"}, w_0, w_1 ; for priors see Table II	$w_0 = 0.09$; $w_1 = 0.33$
AU, MI, PJS	8 yr. WMAP + 2200 SNe + W L	\textit{"vanilla"}, w_0, w_1 ; for priors see Table II	$w_0 = 0.07$; $w_1 = 0.18$

TABLE V III: Forecast 1 constraints on the dark energy equation of state. (The "vanilla" parameter space is spanned by the six parameters ($h, !_m, !_b, \text{de}, 8, A, n_s$).

Table IX lists the new constraints obtained. The standard deviations in our original constraints are about 10%, so we did not consider a model variation to be significant unless it changed constraints by at least 20% – 30%. First we checked to what extent a CM B simulation without the "extra" factor of f_{sky} in the denominator of the covariance matrix (12, 13, 14, 15, 16, 17, 18) would improve our constraints. The difference turns out to be negligible.

Probes	Analysis	$w_0(2)$	$w_1(2)$
SN Ia	prior $m = 0.31$	0.182	0.0037
CMB + SN Ia	standard	0.19	0.018
	$f_{\text{sky}}^2 \neq f_{\text{sky}}$ in (12-18)	0.19	0.70
	CMB 1 400	0.18	0.67
	1 yr. WMAP	0.19	0.82
	$SN_m = 0.1$	0.064	0.42
	$SN_m = 0.3$	0.41	0.83
CMB + SN Ia + WL	standard	0.12	0.007
	WL on linear scales only	0.18	0.57
	CMB 1 400	0.15	0.32

TABLE IX: Consistency checks of our dark energy constraints. All constraints shown are at the 2 level, with the standard deviations in constraints from multiple Monte Carlo simulations shown when available. The "standard" analyses are those described in Sections IIIB, IIIC, and IIID, while the other analyses differ from the standard ones as specified in the Analysis column.

In fact, the final constraints are relatively independent of the details of the CMB simulation and analysis. Cutting off the CMB power spectrum at a maximum multipole of 400, or replacing the WMAP 8 year data set with a simulated 1 year data set, lead to insignificant changes in the dark energy constraints. On the other hand, the constraints are very sensitive to changes in the quality of the supernova data. Changing the SN Ia magnitude uncertainty leads to significant changes in the dark energy constraints. Meanwhile, the final 2 uncertainties provided by the combination of CMB and SN Ia data are nearly identical to those found by fixing m in the SN analysis alone. Thus, in some sense, adding the CMB data set is equivalent to fixing m as a function of w_0 and w_1 in the supernova analysis.

We began Sec. IV C by identifying two milestones for comparing constraints on w_0 and w_1 . The first milestone, to distinguish between CDM and tracking models of dark energy, is not quite reached by the combination of CMB and SN Ia data sets. We found $w(0.3)(2) = 0.12$, slightly larger than the uncertainty of 0.1 needed to reach this milestone. Since that 2 bound is itself uncertain by

10%, the actual bounds obtained may be even wider, thus we cannot confidently claim that the combination of CMB and SN Ia data can distinguish between CDM and trackers. Also, this combination is insufficient to reach the second milestone, which would require that the uncertainties in w_0 and w_1 be reduced by at least an order of magnitude.

The addition of weak lensing to the analysis resulted in the contours shown in Fig. 19, with grid spacings $w_0 = 0.04$ and $w_1 = 0.1$. Weak lensing tightened the 1 constraints to $w_0 = 0.07$ and $w_1 = 0.18$, and the 2 constraints to $w_0(2) = 0.12$ and $w_1(2) = 0.29$. We checked our results using a Fisher matrix calculation and found the 1 constraints $w_0 = 0.05$ and $w_1 = 0.16$, con-

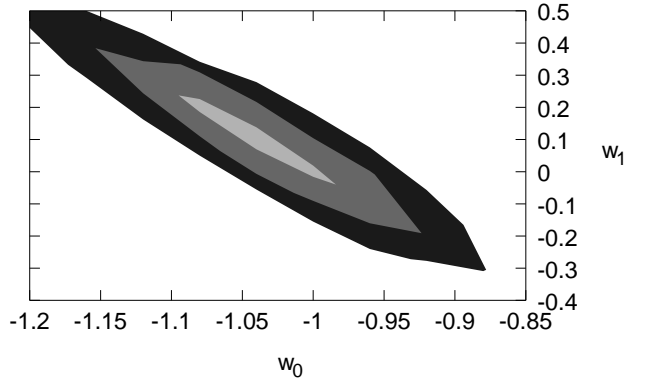


FIG. 19: Forecast CMB, SN Ia, and WL constraints on dark energy. The 1 contour (light gray), the 2 contour (dark gray), and the 3 contour (black) are shown.

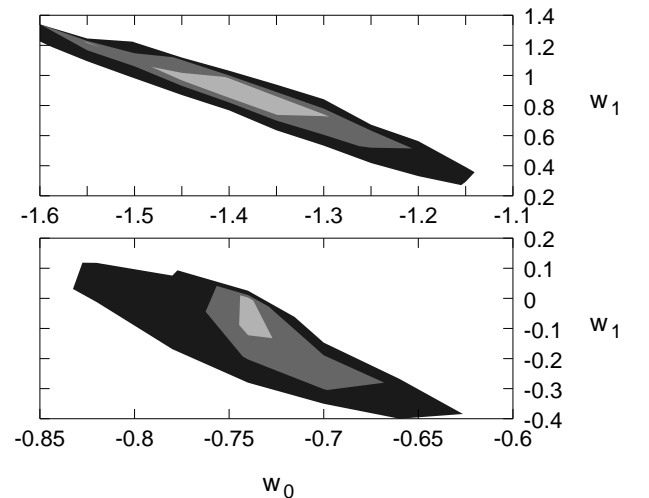


FIG. 20: 2 contours for CMB, SN Ia, and WL "data" simulated using the fiducial models ($w_0 = 1.3, w_1 = 0.5$) (top) and ($w_0 = 0.7, w_1 = 0.3$) (bottom). The 1 contours (light gray), 2 contours (dark gray), and 3 contours (black) are shown.

sistent with our minimization results. Our constraints are tighter than those forecast for SNAP SNe Ia with Planck priors, but worse than SNAP SNe Ia with weak lensing, as listed in Table V III. Meanwhile, galaxy cluster measurements based on the more ambitious LSST survey claim an improvement by factors of 3–5 over our forecasts, depending on the number of clusters assumed [41].

Once again, four more simulated datasets were analyzed to test the robustness of our constraints. The mean 2 uncertainties in w_0 and w_1 were 0.11 and 0.27, respectively, and the standard deviations in the 2 constraints were 0.007 and 0.030, respectively. As before, our constraints on w_0 and w_1 are each correct to about 10%, demonstrating the reliability of our forecasts.

Repeating the analysis with two different fiducial models suggested a strong dependence of the contours on the choice of fiducial model. Fig. 20 shows the χ^2 contours for the fiducial models ($w_0 = 1.3, w_1 = 0.5$) and ($w_0 = 0.7, w_1 = 0.3$). The first of these models had 2 uncertainties of 0.19 and 0.41 in w_0 and w_1 , respectively. The second had 2 uncertainties of 0.05 and 0.19 in w_0 and w_1 , respectively. Since these constraints are more than 2-3 standard deviations away from the mean constraints for the ($w_0 = 1, w_1 = 0$) fiducial model, the constraints must be dependent on the fiducial model. Moving along the degeneracy direction from the lower right of the cosmological constant model ($w_0 > 1, w_1 < 0$) to the upper left ($w_0 < 1, w_1 > 0$) results in larger contours. However, we stress that these findings are not yet conclusive. Only one simulated data set was analyzed for each of two alternative fiducial models. A study employing multiple Monte Carlo realizations and several fiducial models would be computationally intensive, and is beyond the scope of this paper.

Further tests of the robustness of our constraints revealed that, once again, CMB data at $l > 400$ do not contribute to the dark energy constraints (see Table IX). Meanwhile, if the weak lensing analysis is restricted to linear scales, then constraints on w_0 and w_1 weaken considerably, as shown in Table IX. This is consistent with the findings of [37].

Comparing 2 constraints with and without weak lensing (including nonlinear scales), we see that the uncertainties on w_0 shrink by about 40%, and the uncertainties on w_1 shrink by 60%. Overall, the area of the 2 contour decreases by 80% due to the addition of weak lensing data.

This improvement allows the combination of CMB, SNIa, and WL data to reach one of the two milestones identified at the beginning of this section. The constraint $w(0.3)(2) = 0.044$ is tight enough that this combination of data can easily distinguish between the cosmological constant and tracker models of dark energy. Thus, weak lensing will allow us to rule out a portion of the most interesting region of parameter space. On the other hand, our forecast dark energy constraints do not reach the second milestone, which calls for these 2 uncertainties to be reduced to 0.025. In particular, the uncertainty in w_1 is higher than this by over an order of magnitude.

We have not included in our analysis either weak lensing tomography or galaxy cluster measurements, which may lower statistical uncertainties even further [41, 114]. These have been analyzed by others and look promising. They suggest that we can approach the second milestone, but there is no method suggested so far for pushing substantially beyond their forecast constraints.

Moreover, we remind the reader that the constraints discussed above, as well as the improvement due to weak lensing, are based on several optimistic assumptions listed at the beginning of Sec. IV C. Systematic effects, such as dust-related dimming of the supernovae, can in-

crease uncertainties in w_0 and w_1 . Also, if the best-fit dark energy model is near the boundary of the (w_0, w_1) parameter space, then $w(z)$ parameterization dependence will further weaken our constraints on the dark energy parameters. In the worst-case scenario $w_0 + w_1 = 0$, the best-fit model will be near the boundary of parameter space; parameterization-related uncertainties in w_0 and $w^0(0)$ could completely swamp any improvements.

V. CONCLUSIONS

The purpose of this investigation has been to determine how well $w(z)$ can be resolved using currently planned astronomical observations. The well-known challenge is that individual measurements do not constrain $w(z)$ directly, but rather some functional that depends on $w(z)$, integrals of $w(z)$, and a large set of additional parameters.

We have shown that the uncertainties in measuring w and dw/dz at $z = 0$ can be reduced dramatically by the beginning of the next decade, using a combination of the highest-quality CMB, SN, and WL data. However, the remaining uncertainties, $w_0(2) = 0.12$ and $w_1(2) = 0.29$, will not be enough to determine definitively whether dark energy is inert (a cosmological constant) or dynamical (quintessence), unless the true value of w differs from 1 by significantly more than 0.1. Unfortunately, many quintessence models have $w_0 + 1 < 0.1$ and $w_1 < 0.1$.

Our numerical studies illustrate how the measurements combine to produce this constraint. Even the best supernova measurements are degenerate under certain combinations of variations in $w(0)$, $w^0(0)$, and m [35]. CMB constraints are degenerate along a surface in the space spanned by $w(0)$, $w^0(0)$, h , and m . However, we have found (Fig. 17) that combining CMB and SN measurements effectively collapses the degeneracy in the m direction, leaving only the degeneracy in the $w(0)$, $w^0(0)$ plane. We have shown that the CMB contribution to this degeneracy breaking comes entirely from the $l > 400$ region of the power spectrum. Since even the first year of WMAP data has reduced uncertainties in this range to near the cosmic variance level, we do not expect a significant improvement in dark energy constraints from further WMAP or Planck CMB data. Of course, this relies on our choice of cosmological parameters, and in particular, our assumption that $\kappa = 0$. If curvature were considered, the angular diameter distance degeneracy would degrade the information on m provided by the first CMB acoustic peak, and better information on subsequent peaks could prove valuable. Also, we have not considered nonlinear effects such as the gravitational lensing of the CMB power spectra [115], which could provide valuable information on structure formation. On the other hand, the m constraints are quite sensitive to the supernova magnitude uncertainties. A 50% change in m changes the 2 constraints on $w(0)$ by at least

a factor of two. After the CM B and SN data sets are combined, the remaining degeneracy runs along curves of $w(z)$ which intersect one another near $z = 0.3$. The uncertainty in $w(0.3)$ is roughly 0.12 at the 2 level, depending on what functional forms for $w(z)$ are considered.

To break the degeneracy between $w(0)$ and $w'(0)$, more data must be co-added that can constrain $w(z)$ at a greater red shift. We have studied the weak lensing power spectrum as a means of breaking the $w(0)$ - $w'(0)$ degeneracy. Our previous conclusion about the highest CM B multipoles remains valid; CM B data at $l > 400$ do not contribute to dark energy constraints even when weak lensing is considered. Furthermore, any improvements due to weak lensing depend crucially on our ability to use shear measurements on nonlinear scales. This will require a better understanding of systematics, such as intrinsic alignments of galaxies, as well as more accurate computations of the matter power spectrum on nonlinear scales in dynamical dark energy cosmologies. When CM B, SN, and WL are combined, the supernovae constrain $w(z)$ at low red shifts $z = 0.3$, while weak lensing constrains $w(z)$ at higher red shifts [40], leading to improvements of nearly a factor of two in w_0 and more than a factor of two in w_1 . Other work has considered highly ambitious surveys of the cluster abundance evolution [41], assuming large numbers of observed clusters, or of weak lensing tomography [114], based on multiple red shift bins and observations of large fractions of the sky. Both probes

measure the structure growth rate as a function of red shift. These have the potential to improve statistical uncertainties significantly, by factors of 3-5 compared with our results, but concerns remain about systematic uncertainties [41, 114]. Even taking the current estimated errors, uncertainties in w_0 and w_1 are several percent, which still allows a range of plausible quintessence models. Thus, unless we are lucky enough to find a dark energy that is very different from the cosmological constant, new kinds of measurements or an experiment more sophisticated than those yet conceived will be needed in order to settle the dark energy issue.

Acknowledgments

We thank N. Bahcall, J. Gunn, C. Hirata, S. Ho, A. Makarov, I. Maor, J. Ostriker, U. Seljak, D. Spergel, C. Stubbs, Y. Wang, and D. Weesley for useful conversations. Our analysis was run on a Beowulf cluster at Princeton University, supported in part by NSF grant AST-0216105. This material is based upon work supported under a National Science Foundation Graduate Research Fellowship (AU). M.I. acknowledges the support of the Natural Sciences and Engineering Research Council of Canada. This work was supported in part by US Department of Energy Grant DE-FG02-91ER40671 (PJS).

[1] A.G. Riess, et al., *Astron. J.* 116, 1009-1038 (1998).
 [2] P.M. Garnavich et al., *Astrophys. J.* 509, 74-79 (1998).
 [3] Alexei V. Filippenko and Adam G. Riess, *Phys. Rept.* 307, 31-44 (1998).
 [4] S. Perlmutter, et al., *Astrophys. J.* 517, 565-586 (1999).
 [5] S. Perlmutter, et al., *Bull. Am. Astron. Soc.* 29, 1351 (1997).
 [6] A.G. Riess, et al., *Astrophys. J.* 536, 62 (2000).
 [7] A.G. Riess, et al., *Astrophys. J.* 560, 49-71 (2001).
 [8] J.L. Tonry, et al., *Astrophys. J.* 594, 1-24 (2003).
 [9] R.A. Knop, et al., *Astrophys. J.* 598, 102-137 (2003).
 [10] B.J. Barris, et al., *Astrophys. J.* 602, 571-594 (2004).
 [11] A.G. Riess, et al., *Astrophys. J.* 607, 665-687 (2004).
 [12] C.L. Bennett, et al., *Astrophys. J. Suppl. Ser.* 148, 1 (2003).
 [13] D.N. Spergel, et al., *Astrophys. J. Suppl. Ser.* 148, 175 (2003).
 [14] W.L. Freedman, et al., *Astrophys. J.* 553, 47-72 (2001).
 [15] M. Tegmark, et al., *Astrophys. J.* 606, 702-740 (2004).
 [16] M. Tegmark, et al., *Phys. Rev. D* 69, 103501 (2004).
 [17] P. Fosalba, E.G. Gaztanaga, and F.C. Castander, *Astrophys. J.* 597, L89-92 (2003).
 [18] P. Fosalba and E.G. Gaztanaga, *Mon. Not. R. Astron. Soc.* 350, L37-L41 (2004).
 [19] R. Scranton, et al., *Phys. Rev. Lett.* (submitted) [[astro-ph/0307335](#)] (2003).
 [20] N. A. Shorodji, Y.-S. Loh, and M.A. Strauss, *Phys. Rev. D* 69, 8, 083524 (2004).
 [21] S. Boughn and R. Crittenden, *Nature*, 427, 45-47 (2004).
 [22] N. Padmanabhan, et al., *Phys. Rev. D* (submitted) [[astro-ph/0410360](#)] (2004).
 [23] P.J.E. Peebles and B. Ratra, *Astrophys. J. Lett.* 325, L17-L20 (1988).
 [24] B. Ratra and P.J.E. Peebles, *Phys. Rev. D* 37, 12, 3406-3427 (1988).
 [25] I. Zlatev, L. Wang, and P.J. Steinhardt, *Phys. Rev. Lett.* 82, 896-899 (1999).
 [26] P.J. Steinhardt, L. Wang, and I. Zlatev, *Phys. Rev. D* 59, 123504 (1999).
 [27] R.R. Caldwell, *Phys. Lett. B* 545, 23-29 (2002).
 [28] S.M. Carroll, M. Hoffman, and M. Trodden, *Phys. Rev. D* 68, 023509 (2003).
 [29] J.R. Bond, et al., *Phys. Rev. Lett.* 72, 13-16 (1994).
 [30] J.R. Bond, G. Efstathiou, and M. Tegmark, *Mon. Not. R. Astron. Soc.* 291, L33-L41 (1997).
 [31] M. Zaldarriaga, D. Spergel, and U. Seljak, *Astrophys. J.* 488, 1-13 (1997).
 [32] M. White, *Astrophys. J.* 506, 495 (1998).
 [33] G. Huey, et al., *Phys. Rev. D* 59, 063005 (1999).
 [34] G. Efstathiou and J.R. Bond, *Mon. Not. R. Astron. Soc.* 304, 75-97 (1999).
 [35] I. Maor, R. Brustein, and P.J. Steinhardt, *Phys. Rev. Lett.* 86, 6-9 (2001).
 [36] W. Hu, *Phys. Rev. D* 65, 023003 (2002).
 [37] D. Huterer, *Phys. Rev. D* 65, 063001 (2002).

[38] G. Aldering, et al., *Publ. Astron. Soc. Pac.* (submitted) [[astro-ph/0405232](#)] (2004). [see also <http://snap.lbl.gov>].

[39] Y.-S. Song and L. Knox, *Phys. Rev. D* (submitted) [[astro-ph/0312175](#)] (2003).

[40] L. Knox, A. Albrecht, and Y.S. Song, [[astro-ph/0408141](#)] (2004).

[41] S. Wang, et. al. *Phys. Rev. D* (submitted) [[astro-ph/0406331](#)] (2004).

[42] D. Huterer and M. S. Turner, *Phys. Rev. D* 64, 123527 (2001).

[43] K. Benabed and L. Van Waerbeke, [[astro-ph/0306033](#)] (2003).

[44] K. Abazajian and S. Dodelson, *Phys. Rev. Lett.* 91 041301 (2003).

[45] A. Refregier et al. [astro-ph/0304419](#) (2003).

[46] A. Heavens, *Mon. Not. Roy. Astron. Soc.* 343 1327 (2003).

[47] P. Simon, L. J. King and P. Schneider, accepted by *A & A*, [[astro-ph/0309032](#)] (2003).

[48] B. Jain and A. Taylor, *Phys. Rev. Lett.* 91 141302 (2003).

[49] G. M. Bernstein, B. Jain, *Astrophys. J.* 600 17 (2004).

[50] W. Jang, et al., *Third Statistical Challenges in Modem Astronomy Conference*, 221-241 (2003).

[51] E. V. Linder, *Phys. Rev. Lett.* 90, 091301 (2003).

[52] U. Seljak, et al., [[astro-ph/0407372](#)] (2004).

[53] R. R. Caldwell, et al., *Astrophys. J.* 591, L75-L78 (2003).

[54] R. R. Caldwell and M. Doran, *Phys. Rev. D* 69, 103517 (2004).

[55] M. Ishak, et al., *Phys. Rev. D* 69, 083514 (2004).

[56] I. Tereno, et al., *Astron. Astrophys.* (submitted) [[astro-ph/0404317](#)] (2004).

[57] M. Ishak, C. Hirata, *Phys. Rev. D* (submitted) [[astro-ph/0405042](#)] (2004).

[58] W. H. Press, S.A. Teukolsky, W. T. Vetterling, and B. P. Flannery, *Numerical Recipes in C: The Art of Scientific Computing*, (Cambridge University Press, Cambridge, 1992).

[59] M. M. Phillips, *Astrophys. J. Lett.* 413, L105-L108 (1993).

[60] M. Hamuy, et al., *Bull. Am. Astron. Soc.* 26, 1362 (1994).

[61] A. G. Riess, W. H. Press, and R. P. Kirshner, *Astrophys. J.* 438, L17-20 (1995).

[62] A. G. Riess, W. H. Press, and R. P. Kirshner, *Astrophys. J.* 473, 88 (1996).

[63] S. Perlmutter, et. al., *Astrophys. J.* 483, 565 (1997).

[64] U. Seljak and M. Zaldarriaga, *Astrophys. J.* 469, 437-444 (1996).

[65] R. Caldwell (private communication).

[66] L. Verde, et al., *Astrophys. J. Suppl. Ser.* 148, 195 (2003).

[67] G. Hinshaw, et al., *Astrophys. J. Suppl. Ser.* 148, 63 (2003).

[68] A. Kogut, et al., *Astrophys. J. Suppl. Ser.* 148, 161 (2003).

[69] <http://www.hep.upenn.edu/~max/sdsspars.html> (2003).

[70] W. M. Wood-Vasey, et al., *New Astron. Rev.* 48, 637-640 (2004).

[71] [http://home.fnal.gov/~annis/astrophys/deCam/proposal/DESBACproposal031104.pdf](http://home.fnal.gov/~annis/astrophys/deCam/PAC04/proposal/DESBACproposal031104.pdf) [[astro-ph/0410501](#)] (2004). [see also <http://home.fnal.gov/~annis/astrophys/deCam/>]

[72] A. G. Kim, et al., *Mon. Not. Roy. Astron. Soc.* 347, 909-920 (2004).

[73] <http://cfht.hawaii.edu/SNLS/> [see also <http://snls.in2p3.fr/conf/posters/AAS203/AAS04SNLS.v4.ppt> for a recent poster].

[74] C. Stubbs (private communication).

[75] D. S. Maddick, et al., *Astrophys. J.* 599, L33-L36 (2003).

[76] R. Pain, et al., *Bull. Am. Astron. Soc.* 34, 1169 (2002).

[77] C. J. Pritchett [[astro-ph/0406242](#)] (2004).

[78] R. C. Smith, et al., *Bull. Am. Astron. Soc.* 34, 1232 (2002).

[79] P. M. G. Lamavich, et al., *Bull. Am. Astron. Soc.* 34, 1233 (2002).

[80] R. P. Kirshner, et al., *American Astronomical Society Meeting* 202 (2003). [see also <http://www.ctio.noao.edu/~wsne>].

[81] J. R. Bond, A. H. Jaffe, and L. Knox, *Astrophys. J.* 533, 19 (2000).

[82] Ya. B. Zeldovich and R. A. Sunyaev, *Astrophys. & Space Sci.*, 4, 301 (1969).

[83] R. A. Sunyaev and Ya. B. Zeldovich, *Comments Astrophys. Space Phys.*, 4, 173 (1972).

[84] A. Blanchard and J. Schneider, *Astron. Astrophys.* 184, 1 (1987).

[85] A. Kashlinsky, *Astrophys. J. Lett.* 331, L1 (1988).

[86] K. M. Hubenberger, U. Seljak, and A. Makarov, [[astro-ph/0404545](#)] (2004).

[87] U. Seljak and C. M. Hirata, *Phys. Rev. D* 69, 043005 (2004).

[88] C. M. Hirata, et al., *Phys. Rev. D* (submitted) [[astro-ph/0406004](#)] (2004).

[89] C. R. Lawrence and A. E. Lange, *Bull. Am. Astron. Soc.* 29, 1273 (1997).

[90] R. J. Laureijs, *International Astronomical Union Symposium* no. 216 (2003).

[91] N. Kaiser, *Astrophys. J.* 388, 272, (1992).

[92] B. Jain and U. Seljak, *Astrophys. J.* 484, 560, (1997).

[93] N. Kaiser, *Astrophys. J.* 498, 26, (1998).

[94] J. M. Bardeen, J. R. Bond, N. Kaiser, and A. S. Szalay, *Astrophys. J.*, 304, 15 (1986).

[95] Chung-Pei Ma, R. R. Caldwell, Paul Bode and Limin Wang, *Astrophys. Letter* 521, 1, (1999).

[96] R. E. Smith, et al. *Mon. Not. R. Astron. Soc.* 341, 1311 (2003).

[97] <http://pan-starrs.ifa.hawaii.edu/public/index.html>.

[98] S. Hannestad and E. Mortsell, [[astro-ph/0407259](#)] (2004).

[99] Y. Wang and M. Tegmark, *Phys. Rev. Lett.* 92, 241302 (2004).

[100] U. Alam, V. Sahni, and A. A. Starobinsky, *JCAP* 0406, 008 (2004).

[101] T. R. Choudhury and T. Padmanabhan, [[astro-ph/0311622](#)] (2003).

[102] D. Rapetti, S. W. Allen, and J. Weller, [[astro-ph/0409574](#)] (2004).

[103] A. Makarov (private communication).

[104] A. Slosar, U. Seljak, and A. Makarov, *Phys. Rev. D*, 69, 123003 (2004).

[105] U. Seljak, et al., [[astro-ph/0406594](#)] (2004).

[106] Y. Wang, *Astrophys. J.*, 531, 676 (2000).

[107] Y. Wang, [[astro-ph/0406635](#)] (2004).

[108] <http://home.fnal.gov/~annis/astrophys/deCam/DESBACproposal031104.pdf> [[astro-ph/0410501](#)] (2004).

[109] I. Zlatev, L. Wang, and P. J. Steinhardt, *Phys. Rev.*

Lett. 82, 896-899 (1999).

[110] P. Brax and J. Martin, Phys. Lett. B 468, 40-45 (1999).

[111] A. Refregier, Ann. Rev. Astron. Astrophys. 41, 645 (2003).

[112] I. Maor, et al., Phys. Rev. D 65, 123003 (2002).

[113] J.-M. Virey, et al., [astro-ph/0407452] (2004).

[114] M. Ishak and D. Spergel (in preparation) (2004).

[115] C. M. Hirata and U. Seljak, Phys. Rev. D 68, 083002 (2003).